

Surrogate Model for Geological CO₂ Storage and Its Use in MCMC-based History Matching

Yifu Han^a, François P. Hamon^b, Su Jiang^a, Louis J. Durlofsky^a

^a*Department of Energy Science and Engineering, Stanford University, Stanford, CA, 94305, USA*

^b*TotalEnergies, E&P Research and Technology, 1201 Louisiana Street, Houston, TX, 77002, USA*

Abstract

Deep-learning-based surrogate models show great promise for use in geological carbon storage operations. In this work we target an important application – the history matching of storage systems characterized by a high degree of (prior) geological uncertainty. Toward this goal, we extend the recently introduced recurrent R-U-Net surrogate model to treat geomodel realizations drawn from a wide range of geological scenarios. These scenarios are defined by a set of metaparameters, which include the mean and standard deviation of log-permeability, permeability anisotropy ratio, horizontal correlation length, etc. An infinite number of realizations can be generated for each set of metaparameters, so the range of prior uncertainty is large. The surrogate model is trained with flow simulation results, generated using the open-source simulator GEOS, for 2000 random realizations. The flow problems involve four wells, each injecting 1 Mt CO₂/year, for 30 years. The trained surrogate model is shown to provide accurate predictions for new realizations over the full range of geological scenarios, with median relative error of 1.3% in pressure and 4.5% in saturation. The surrogate model is incorporated into a

Markov chain Monte Carlo history matching workflow, where the goal is to generate history matched realizations and posterior estimates of the meta-parameters. We show that, using observed data from monitoring wells in synthetic ‘true’ models, geological uncertainty is reduced substantially. This leads to posterior 3D pressure and saturation fields that display much closer agreement with the true-model responses than do prior predictions.

Keywords: geological carbon storage, surrogate model, deep learning, MCMC, history matching, GEOS

1. Introduction

Geological carbon storage, if implemented at the gigatonne scale, has the potential to significantly reduce atmospheric CO₂ emissions. There are, however, many challenges associated with modeling and optimizing large-scale carbon storage operations. For example, because significant uncertainty exists in the detailed distributions of aquifer properties, model calibration is an essential step in the workflow. This calibration (also referred to as history matching or data assimilation), however, requires numerous time-consuming flow simulations, which must be repeated as new data are collected. Very fast data-driven surrogate models, used in place of these high-fidelity flow simulations, have been shown to provide accurate solutions at reduced computational cost for idealized cases. Their extension and application for more realistic scenarios, however, remains an open issue.

In recent work, a deep-learning-based surrogate model that uses residual U-Nets within a recurrent neural network architecture was developed to predict flow and surface displacement in carbon storage models (Tang et al.,

2022a). This surrogate model treated 3D multi-Gaussian permeability realizations drawn from a single (specified) geological scenario. This means the geomodels were all characterized by the same scenario-defining quantities. Examples of scenario-defining quantities, also referred to as metaparameters, are the mean and standard deviation of porosity and log-permeability, the (spatial) correlation lengths in three orthogonal directions, the ratio of vertical to horizontal permeability, etc. In practice these metaparameters are themselves uncertain, so it is important to include them as variables in the history matching procedure. In this study, we extend the recurrent R-U-Net surrogate model to treat geomodel realizations drawn from a wide range of geological scenarios. The surrogate model is then used with a Markov chain Monte Carlo history matching procedure to reduce uncertainty in the metaparameters and thus in predicted pressure and saturation fields.

A number of deep-learning-based surrogate models have been developed to estimate flow quantities in carbon storage applications. Mo et al. (2019) introduced a data-driven deep convolutional encoder-decoder network to predict pressure and saturation for 2D Gaussian permeability fields. Wen et al. (2021) presented a temporal convolutional neural network to predict pressure and saturation for single-well axisymmetric injection scenarios. Wen et al. (2023) later proposed an nested Fourier neural operator (FNO) for 3D problems. This architecture enables predictions of saturation and pressure in cases with permeability and porosity heterogeneity and anisotropy, under different reservoir conditions and injection-well configurations. Yan et al. (2022a) developed an FNO-based surrogate model to predict saturation and pressure, in both injection and post-injection periods, for new permeability

and porosity fields and operational settings. Yan et al. (2022b) proposed a physics-informed deep neural network model for CO₂ storage problems. They added flux terms into the loss function (minimized during training) to improve the resulting pressure fields. Tang et al. (2022a) extended earlier recurrent R-U-Net surrogate models (Tang et al., 2020, 2021) to treat coupled flow and geomechanics. Their surrogate provided predictions for flow variables in the storage aquifer, along with vertical displacement at the Earth's surface (for new realizations drawn from a single geological scenario).

A variety of history matching procedures have been applied in previous studies. Chen et al. (2020) incorporated pressure and saturation data from monitoring wells to reduce uncertainty in predictions of saturation and pressure at plugged/abandoned wells. Tavakoli et al. (2013) used pressure at the injection well and saturation at the monitoring well to reduce uncertainty in the location of the saturation plume. Xiao et al. (2022) used saturation fields interpreted from time-lapse seismic data to history match permeability. Liu and Grana (2020) integrated injection well bottom-hole pressure, saturation at the monitoring wells, and time-lapse seismic data to reduce uncertainty in porosity and permeability fields and thus plume location. Jung et al. (2015) used pressure data from both the storage aquifer and the caprock to detect potential leakage pathways. González-Nicolás et al. (2015) applied a restart ensemble Kalman filter algorithm with pressure measurements above the storage aquifer to identify caprock discontinuities. Jahandideh et al. (2021) considered coupled flow and geomechanics, and used microseismic data to history match permeability and geomechanical parameters. It is important to note that none of studies mentioned above considered uncertainty in the

geological scenario, i.e., in the metaparameters. This could be extremely expensive with these approaches because they are all simulation-based.

Surrogate models have been widely used for history matching and uncertainty quantification in many types of subsurface flow problems. Wang et al. (2021) developed a theory-guided neural network approach for efficient Monte Carlo-based uncertainty quantification in subsurface hydrology problems. Zhou and Tartakovsky (2021) proposed a surrogate-based adaptive MCMC method to reduce uncertainty in parameters characterizing the initial contaminant plume in groundwater problems. Jiang and Durlofsky (2023) proposed a transfer-learning framework that used low and high-fidelity simulation data to train their surrogate model. The surrogate was then used in an ensemble-based history matching procedure in the context of oil reservoir simulation. Surrogate models have also been used for history matching in geological carbon storage problems. Mo et al. (2019) used a surrogate model for uncertainty quantification in this setting. Tang et al. (2022a) incorporated their surrogate model with a rejection sampling-based history matching procedure to reduce uncertainty in aquifer pressure and surface displacement. Similarly, Tang et al. (2022b) considered ensemble-based history matching, with surrogate-based flow predictions, to history match porosity and permeability.

The main goals of this study are two-fold. First, we extend the recurrent R-U-Net surrogate model to treat geological realizations drawn from multiple geological scenarios, with each scenario characterized by a distinct set of metaparameters. Second, we use the surrogate model in a formal MCMC-based data assimilation workflow, in which we construct posterior (history

matched) predictions for the metaparameters. To our knowledge, this is the first MCMC treatment involving multiple geological scenarios (and metaparameters) applied within the context of geological carbon storage. The metaparameters considered in this study include mean and standard deviation of the 3D multi-Gaussian log-permeability field, permeability anisotropy ratio, correlation length, and constants in the porosity-permeability relationship. These are sampled from broad prior distributions to provide training realizations. Flow simulations, performed using the open-source simulator GEOS (Bui et al., 2021), provide the 3D pressure and saturation fields required for training. New input channels are introduced in the recurrent R-U-Net model to handle multiple geological scenarios. The MCMC method involves a random walk Metropolis sampling algorithm, with a randomly selected metaparameter modified at each iteration. Results for two different (synthetic) ‘true’ models demonstrate the ability of the overall framework to provide substantial uncertainty reduction in key metaparameters, leading to higher accuracy in flow predictions.

This paper proceeds as follows. The metaparameters and procedure to construct geomodels are presented in Section 2. In Section 3, we first discuss flow simulations using GEOS. The extended recurrent R-U-Net surrogate model is then described. In Section 4, our MCMC-based history matching procedure is presented. Flow predictions for 3D models, and comparisons to high-fidelity simulation results, are provided in Section 5. The problem setup involves 4 megatonnes/year of CO₂ injection through four vertical wells. MCMC-based history matching results are presented in Section 6. We conclude in Section 7 with a summary and suggestions for future work.

2. Geomodels and Metaparameters

The flow simulations are performed on an overall domain consisting of a storage aquifer and a surrounding region, as shown in Fig. 1. The dimensions of the full system are $120 \text{ km} \times 120 \text{ km} \times 100 \text{ m}$. The storage aquifer, of size $12 \text{ km} \times 12 \text{ km} \times 100 \text{ m}$, is at the center of the model. The storage aquifer is represented by $80 \times 80 \times 20$ cells and the overall domain by $100 \times 100 \times 20$ cells. The cells in the storage aquifer are $150 \text{ m} \times 150 \text{ m} \times 5 \text{ m}$. The cells in the surrounding domain increase in size (in x and y) with distance from the storage aquifer.

The geomodels of the full system are denoted by $\mathbf{m}_f \in \mathbb{R}^{n_c \times n_p}$, where $n_c = 200,000$ is the number of cells in the overall domain, and $n_p = 3$ is the number of rock properties in each cell (horizontal permeability, porosity, and permeability anisotropy ratio). The rock properties in the surrounding domain are taken to be constant. The geomodel realizations of the storage aquifer are drawn from a range of geological scenarios characterized by a set of six metaparameters. The metaparameters $\boldsymbol{\Theta}_{\text{meta}} \in \mathbb{R}^6$ are given by

$$\boldsymbol{\Theta}_{\text{meta}} = [l_h, \mu_{\log k}, \sigma_{\log k}, a_r, d, e], \quad (1)$$

where k indicates the horizontal permeability, l_h denotes the horizontal correlation length, $\mu_{\log k}$ and $\sigma_{\log k}$ are the mean and standard deviation of the log-permeability field, a_r is the permeability anisotropy ratio ($a_r = k_v/k$, where k_v is vertical permeability), and d and e are coefficients relating porosity to permeability. For any set of metaparameters, an infinite number of realizations can be generated.

The permeability fields of the storage aquifer are denoted by $\mathbf{k}_s \in \mathbb{R}^{n_s}$, where $n_s = 128,000$ is the number of cells in the storage aquifer. These fields are constructed from standard multi-Gaussian fields $\mathbf{y}^G \in \mathbb{R}^{n_s}$ and the metaparameters, $\mu_{\log k}$ and $\sigma_{\log k}$. During the history matching (online) computations, these multi-Gaussian fields are generated using principal component analysis (PCA). This is much faster and more convenient than using geological modeling software, since several million geomodels must be generated and evaluated for MCMC-based history matching. Given the PCA representation and the other metaparameters, the full geomodel can be constructed.

In the pre-processing (offline) step, required to construct the PCA representation, the standard multi-Gaussian fields are generated using Gaussian sequential simulation in SGeMS (Remy et al., 2009). We use an exponential variogram model characterized by horizontal (x and y) and vertical correlation lengths. The horizontal correlation length (l_h) is a metaparameter, while the vertical correlation length (l_v) is set to 10 m (2 cells).

Because a different PCA basis matrix is required for each possible value of l_h , we consider a discrete set of values for this metaparameter. All other metaparameters are treated as continuous within specified ranges. A PCA basis matrix, denoted Φ_c , $c = 1, \dots, N_c$, is constructed for each of the N_c different values of l_h . In this study, we take $N_c = 5$. Each basis matrix is constructed by performing singular value decomposition on a set of 1000 centered SGeMS realizations, all of which are characterized by a particular l_h value. The left singular vectors and singular values provide the basis matrix Φ_c . The other metaparameters act to shift and rescale the correlated multi-

Gaussian fields provided by PCA.

For a particular correlation length, new PCA realizations of standard multi-Gaussian fields, denoted $\mathbf{y}_c^{\text{pca}} \in \mathbb{R}^{n_s}$, can be generated through application of

$$\mathbf{y}_c^{\text{pca}} = \Phi_c \boldsymbol{\xi} + \bar{\mathbf{y}}_c, \quad (2)$$

where $\Phi_c \in \mathbb{R}^{n_s \times n_d}$ is the basis matrix truncated to n_d columns, $\bar{\mathbf{y}}_c \in \mathbb{R}^{n_s}$ is the mean of the SGeMS realizations used to generate Φ_c , and $\boldsymbol{\xi} \in \mathbb{R}^{n_d}$ is the low-dimensional standard-normal variable. Here n_d is set to 900, which preserves about 95% of the total ‘energy’ present in the original set of 1000 SGeMS realizations (energy here is computed as the sum of the squared singular values). In this study, Φ_c matrices are computed for l_h values of 1500 m, 2250 m, 3000 m, 3750 m and 4500 m, which correspond to 10, 15, 20, 25 and 30 cells. For more details on PCA basis matrix construction, please see Liu and Durlofsky (2021).

For a given cell i in the storage aquifer, the permeability $(k_s)_i$ is given by

$$(k_s)_i = \exp(\sigma_{\log k} \cdot (y^G)_i + \mu_{\log k}), \quad i = 1, 2, \dots, n_s. \quad (3)$$

Note that in the history matching computations, $(y^G)_i$ in Eq. 3 is replaced by $(y_c^{\text{pca}})_i$. The porosity field in the storage aquifer, denoted $\phi_s \in \mathbb{R}^{n_s}$, is generated directly from the permeability field via the metaparameters d and e . The porosity-permeability relationship is expressed as

$$(\phi_s)_i = d \cdot \log((k_s)_i) + e, \quad i = 1, 2, \dots, n_s. \quad (4)$$

The geomodel for the storage aquifer, $\mathbf{m}_s(\boldsymbol{\theta}_{\text{meta}}) \in \mathbb{R}^{n_s \times n_p}$, is defined by the permeability field, the porosity field, and the permeability anisotropy ratio. These models are expressed as

$$\mathbf{m}_s(\boldsymbol{\theta}_{\text{meta}}) = [\mathbf{k}_s, \boldsymbol{\phi}_s, \mathbf{a}_r], \quad (5)$$

where $\mathbf{a}_r \in \mathbb{R}^{n_s}$ defines the permeability anisotropy ratio in every storage aquifer cell. In this study, we treat the anisotropy ratio as an uncertain meta-parameter, which is taken to be constant throughout the storage aquifer.

3. Deep-learning-based Surrogate Model

The high-fidelity flow simulations are performed using the open-source simulator GEOS (Bui et al., 2021). GEOS is able to model coupled flow and geomechanics, though the simulation times are considerably longer if geomechanical effects are included (which is why we consider only flow in this study). For the governing equations for CO₂-water flow simulations, please refer to Tang et al. (2022a).

The flow simulations can be represented as

$$[\mathbf{P}_f, \mathbf{S}_f] = f(\mathbf{m}_f), \quad (6)$$

where f denotes the high-fidelity flow simulation, and $\mathbf{P}_f \in \mathbb{R}^{n_c \times n_{ts}}$ and $\mathbf{S}_f \in \mathbb{R}^{n_c \times n_{ts}}$ are the pressure and saturation in each cell of the overall domain at n_{ts} simulation time steps. The flow simulations are performed for a wide range of geomodels \mathbf{m}_f , with the well locations and operational settings the same in all runs. Specifically, in this study supercritical CO₂ is injected

through four vertical wells, with each well injecting 1 megatonne (Mt) CO₂ per year for 30 years.

We now describe the extended recurrent R-U-Net surrogate model used to approximate the flow variables for new geomodels. The surrogate models are trained to predict saturation and pressure fields only in the storage aquifer (not in the full domain), and only at particular time steps. Separate surrogate models are used for the pressure and saturation fields. In analogy to Eq. 6, the surrogate model predictions can be expressed as

$$[\hat{\mathbf{P}}_s, \hat{\mathbf{S}}_s] = \hat{f}(\mathbf{m}_s; \mathbf{w}), \quad (7)$$

where \hat{f} denotes the surrogate model, $\hat{\mathbf{P}}_s \in \mathbb{R}^{n_s \times n_t}$ and $\hat{\mathbf{S}}_s \in \mathbb{R}^{n_s \times n_t}$ are surrogate model predictions for pressure and saturation in the storage aquifer, n_t is the number of surrogate model time steps, and \mathbf{w} represents the deep neural network parameters determined during training. In this work we take $n_t = 10$. This is considerably less than n_{ts} , though it is sufficient to describe the key dynamics of the storage operation.

The surrogate model, which represents an extension of the recurrent R-U-Net developed by Tang et al. (2022a), contains two main components – a residual U-Net and a recurrent neural network. The residual U-Net, shown in Fig. 2(a), consists of encoding and decoding networks. The encoding network accepts three input channels representing the geomodel. These are transformed to a sequence of low-dimensional latent feature maps, represented as $\mathbf{F}_1, \mathbf{F}_2, \dots, \mathbf{F}_5$. In the decoding network, these latent feature maps are combined with upsampled feature maps through a concatenation process. This provides predictions for the pressure and saturation fields at a

specific time step.

To capture the temporal dynamics, a convolutional long short-term memory (convLSTM) recurrent neural network is incorporated. This network, shown in Fig. 2(b), sequentially applies a time sequence of the most compressed (global) feature maps, denoted $\mathbf{F}_5^1, \dots, \mathbf{F}_5^{n_t}$, through the convLSTM module. The decoding network of the overall surrogate model combines the feature maps from the encoding network ($\mathbf{F}_1 - \mathbf{F}_4$) with each of the \mathbf{F}_5 feature maps to provide pressure and saturation predictions at n_t time steps.

The original surrogate model developed by Tang et al. (2022a) treated geomodels drawn from a single geological scenario that were fully characterized by a single parameter in each cell. Thus only a single input channel was required. Here we consider a wide range of geological scenarios with geomodels characterized by three values in each grid block ($k_i, \phi_i, (a_r)_i$). Thus, three input channels (evident in Fig. 2) and a modified architecture are required.

In particular, in the first convolutional layer, filters are applied to process all three input channels simultaneously. This provides latent feature maps \mathbf{F}_1 that contain the combined features from the three input fields. These \mathbf{F}_1 maps are (again) downsampled in the encoding network into a sequence of low-dimensional latent feature maps $\mathbf{F}_2, \dots, \mathbf{F}_5$. The recurrent component of the network is essentially unchanged, again generating a time sequence of latent feature maps. Details of the extended recurrent R-U-Net architecture are provided in Table 1. Recall that, in our storage aquifer models, $n_x = n_y = 80$ and $n_z = 20$, where n_x , n_y and n_z are the number of cells in each coordinate direction.

We now describe the training procedure. As noted earlier, separate net-

works are trained for pressure and saturation. Scaling and normalization is required prior to training. The log-permeability, porosity, and permeability anisotropy ratio input fields are normalized by scaling based on their respective maximum values. Saturation values are already in the (0, 1) range, so normalization is not required. A (time-dependent) min-max normalization procedure is applied for pressure. The normalized pressure is computed using

$$(\bar{p}_s)_{i,j}^t = \frac{(p_s)_{i,j}^t - (p_s)_{i,j}^0}{(p_s)_{\max}^t - (p_s)_{\min}^t}, \quad (8)$$

where $(p_s)_{i,j}^t$, $(\bar{p}_s)_{i,j}^t$ and $(p_s)_{i,j}^0$ are the pressure, normalized pressure and initial hydrostatic pressure of cell j in geomodel i , at time step t , and $(p_s)_{\max}^t$ and $(p_s)_{\min}^t$ are the maximum and minimum pressure in the storage aquifer at time step t over all pressure fields in all training runs.

The training procedure entails determining optimal network parameters, denoted \mathbf{w}^* , that minimize the difference between flow simulation results and surrogate model predictions. Flow simulations are performed on geomodels sampled from a range of geological scenarios, as explained above. The minimization problem can be stated as

$$\mathbf{w}^* = \underset{\mathbf{w}}{\operatorname{argmin}} \frac{1}{n_{smp}} \frac{1}{n_t} \sum_{i=1}^{n_{smp}} \sum_{t=1}^{n_t} \|\hat{\mathbf{x}}_i^t - \mathbf{x}_i^t\|_2^2, \quad (9)$$

where n_{smp} is the number of training samples (runs), and \mathbf{x}_i^t and $\hat{\mathbf{x}}_i^t$ represent the normalized pressure or saturation from high-fidelity flow simulation and the surrogate model at time step t for training sample i , respectively. In this study we set $n_{smp} = 2000$. The training procedure for pressure requires 22 hours (corresponding to 300 epochs) to converge, while training for satu-

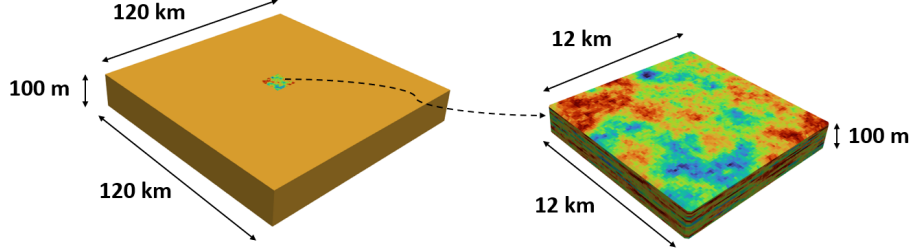
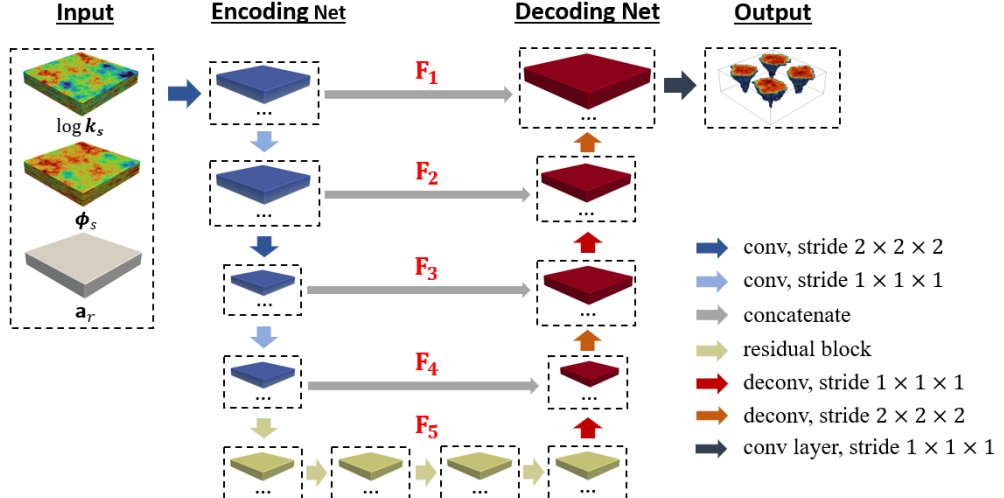


Figure 1: Model domains for flow simulations. Full domain including surrounding region shown on the left, central storage aquifer shown on the right.

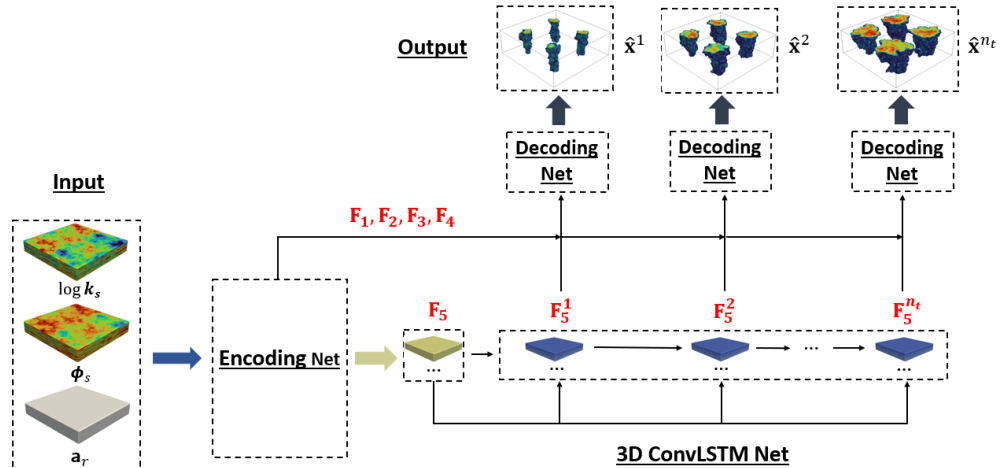
ration requires 37 hours (500 epochs). For both networks a batch size of 4 is used, and the initial learning rate is set to 0.003.

Table 1: Architecture of the extended recurrent R-U-Net

Network	Layer	Output
Encoder	Input	$(n_x, n_y, n_z, 3)$
	conv, 16 filters of size $3 \times 3 \times 3$, stride 2	$(\frac{n_x}{2}, \frac{n_y}{2}, \frac{n_z}{2}, 16)$
	conv, 32 filters of size $3 \times 3 \times 3$, stride 1	$(\frac{n_x}{2}, \frac{n_y}{2}, \frac{n_z}{2}, 32)$
	conv, 32 filters of size $3 \times 3 \times 3$, stride 2	$(\frac{n_x}{4}, \frac{n_y}{4}, \frac{n_z}{4}, 32)$
	conv, 64 filters of size $3 \times 3 \times 3$, stride 1	$(\frac{n_x}{4}, \frac{n_y}{4}, \frac{n_z}{4}, 64)$
	residual block, 64 filters of size $3 \times 3 \times 3$, stride 1	$(\frac{n_x}{4}, \frac{n_y}{4}, \frac{n_z}{4}, 64)$
	residual block, 64 filters of size $3 \times 3 \times 3$, stride 1	$(\frac{n_x}{4}, \frac{n_y}{4}, \frac{n_z}{4}, 64)$
ConvLSTM	convLSTM3D, 64 filters of size $3 \times 3 \times 3$, stride 1	$(\frac{n_x}{4}, \frac{n_y}{4}, \frac{n_z}{4}, 64, n_t)$
Decoder	residual block, 64 filters of size $3 \times 3 \times 3$, stride 1	$(\frac{n_x}{4}, \frac{n_y}{4}, \frac{n_z}{4}, 64, n_t)$
	residual block, 64 filters of size $3 \times 3 \times 3$, stride 1	$(\frac{n_x}{4}, \frac{n_y}{4}, \frac{n_z}{4}, 64, n_t)$
	deconv, 64 filters of size $3 \times 3 \times 3$, stride 1	$(\frac{n_x}{4}, \frac{n_y}{4}, \frac{n_z}{4}, 64, n_t)$
	deconv, 32 filters of size $3 \times 3 \times 3$, stride 2	$(\frac{n_x}{2}, \frac{n_y}{2}, \frac{n_z}{2}, 32, n_t)$
	deconv, 32 filters of size $3 \times 3 \times 3$, stride 1	$(\frac{n_x}{2}, \frac{n_y}{2}, \frac{n_z}{2}, 32, n_t)$
	deconv, 16 filters of size $3 \times 3 \times 3$, stride 2	$(n_x, n_y, n_z, 16, n_t)$
	conv layer, 1 filters of size $3 \times 3 \times 3$, stride 1	$(n_x, n_y, n_z, 1, n_t)$



(a) 3D residual U-Net architecture



(b) Recurrent R-U-Net architecture

Figure 2: Schematic of the 3D recurrent R-U-Net architecture. 3D R-U-Net architecture for pressure and saturation prediction at a specific time step is shown in (a). Incorporation of 3D R-U-Net within recurrent neural network shown in (b). Geomodels are defined by three input channels.

4. Markov Chain Monte Carlo History Matching Procedure

The probability density function for the metaparameters $\boldsymbol{\theta}_{\text{meta}}$, conditioned to observation data, is given by Bayes' theorem:

$$p(\boldsymbol{\theta}_{\text{meta}}|\mathbf{d}_{\text{obs}}) = \frac{p(\boldsymbol{\theta}_{\text{meta}})p(\mathbf{d}_{\text{obs}}|\boldsymbol{\theta}_{\text{meta}})}{p(\mathbf{d}_{\text{obs}})}. \quad (10)$$

Here \mathbf{d}_{obs} represents the observation data, $p(\boldsymbol{\theta}_{\text{meta}}|\mathbf{d}_{\text{obs}})$ is the posterior probability density function, $p(\boldsymbol{\theta}_{\text{meta}})$ is the prior probability density function, $p(\mathbf{d}_{\text{obs}}|\boldsymbol{\theta}_{\text{meta}})$ is the likelihood function, and $p(\mathbf{d}_{\text{obs}})$ is a normalization constant. The determination of the normalization constant would require integrating over the entire metaparameter space, i.e., computing $p(\mathbf{d}_{\text{obs}}) = \int (p(\boldsymbol{\theta}_{\text{meta}}) p(\mathbf{d}_{\text{obs}}|\boldsymbol{\theta}_{\text{meta}})) d\boldsymbol{\theta}_{\text{meta}}$. This expensive calculation is not required in MCMC sampling, as the algorithm enables the estimation of $p(\boldsymbol{\theta}_{\text{meta}}|\mathbf{d}_{\text{obs}})$ without the need to compute the normalization constant.

MCMC sampling is a rigorous method for obtaining samples from posterior distributions. With enough samples, the distributions can be approximated accurately. MCMC involves simulating a Markov chain of a specified length to generate a sequence of samples. In this work, we apply the random walk Metropolis sampling algorithm (Metropolis et al., 1953; Hastings, 1970). The algorithm starts with a random walk in the metaparameter space. The starting set of metaparameters $\boldsymbol{\theta}_{\text{meta}}^1$ is sampled from the prior distributions. In this study these are assumed to be (noninformative) uniform distributions. At each step of the Markov chain, a proposed metaparameter sample $\boldsymbol{\theta}'_{\text{meta}}$ is generated by introducing a random perturbation to the current sample of $\boldsymbol{\theta}_{\text{meta}}^k$ (here k indicates iteration).

The Metropolis-Hastings (Hastings, 1970) acceptance criterion is then applied. The probability of acceptance (denoted by α) for the proposed sample is given by

$$\alpha(\boldsymbol{\theta}_{\text{meta}}^k, \boldsymbol{\theta}'_{\text{meta}}) = \min \left(1, \frac{p(\boldsymbol{\theta}'_{\text{meta}}) p(\mathbf{d}_{\text{obs}} | \boldsymbol{\theta}'_{\text{meta}})}{p(\boldsymbol{\theta}_{\text{meta}}^k) p(\mathbf{d}_{\text{obs}} | \boldsymbol{\theta}_{\text{meta}}^k)} \right), \quad (11)$$

where $p(\mathbf{d}_{\text{obs}} | \boldsymbol{\theta}_{\text{meta}}^k)$ and $p(\mathbf{d}_{\text{obs}} | \boldsymbol{\theta}'_{\text{meta}})$ are the likelihood of the current ($\boldsymbol{\theta}_{\text{meta}}^k$) and proposed ($\boldsymbol{\theta}'_{\text{meta}}$) metaparameters, and $p(\boldsymbol{\theta}_{\text{meta}}^k)$ and $p(\boldsymbol{\theta}'_{\text{meta}})$ are their prior probabilities. The likelihoods are computed from the mismatch between observed and predicted data (the detailed expression will be given in Section 6.1). Given that the prior distributions are uniform, the prior probabilities $p(\boldsymbol{\theta}_{\text{meta}}^k)$ and $p(\boldsymbol{\theta}'_{\text{meta}})$ are equal, resulting in the cancellation of this ratio. By iteratively repeating this sampling procedure, a set of samples that approximates the metaparameter posterior distribution can be generated.

MCMC may require millions of function evaluations to evaluate the likelihoods, which would be computationally prohibitive if the high-fidelity flow simulations were used. With the surrogate model used instead of the high-fidelity simulation, however, the computational cost is manageable. We now describe the detailed MCMC history matching with surrogate modeling used for function evaluations.

The history matching workflow is shown in Algorithm 1. The accuracy and efficiency of the MCMC algorithm is affected by the choice of the proposal distributions. At each step of the Markov chain, one of the six metaparameters (denoted $(\boldsymbol{\theta}_{\text{meta}})_i^k$, $i \in \{1, 2, \dots, 6\}$) is randomly selected for modification. We perturb or sample one metaparameter at a time to reduce the corre-

Algorithm 1: MCMC-based history matching procedure

1. Set iteration counter $k = 1$, and initialize the Markov chain with $\boldsymbol{\theta}_{\text{meta}}^1$.
- repeat**
 2. At each iteration, randomly select a metaparameter i ($i \in \{1, 2, \dots, 6\}$), of value $(\boldsymbol{\theta}_{\text{meta}})_i^k$, to update.
 3. Sample $\boldsymbol{\xi}$ in Eq. 2 from standard normal distribution $\mathcal{N}(0, 1)$.
 4. Construct PCA realization of multi-Gaussian field $\mathbf{y}_c^{\text{pca}}$ using Eq. 2.
 5. Propose a new sample for the metaparameter i , $(\boldsymbol{\theta}_{\text{meta}})'_i$, from its proposal distribution $\mathcal{N}\left((\boldsymbol{\theta}_{\text{meta}})_i^k, \sigma_i^2\right)$.
 6. Construct geomodel $\mathbf{m}_s(\boldsymbol{\theta}'_{\text{meta}})$ based on the newly proposed metaparameters $\boldsymbol{\theta}'_{\text{meta}}$ using Eqs. 3, 4 and 5.
 7. Predict pressure and saturation at n_t time steps using the surrogate models, i.e., through application of $\mathbf{d}' = \hat{f}(\mathbf{m}_s(\boldsymbol{\theta}'_{\text{meta}}))$. Compute likelihood based on mismatch between observed and predicted data (detailed expressions given later). Calculate acceptance probability $\alpha(\boldsymbol{\theta}_{\text{meta}}^k, \boldsymbol{\theta}'_{\text{meta}})$ using Eq. 11.
 8. Sample a random number u from uniform distribution $U(0, 1)$:
if $u \leq \alpha(\boldsymbol{\theta}_{\text{meta}}^k, \boldsymbol{\theta}'_{\text{meta}})$ **then**
 accept $\boldsymbol{\theta}'_{\text{meta}}$, and set $\boldsymbol{\theta}_{\text{meta}}^{k+1} = \boldsymbol{\theta}'_{\text{meta}}$,
else
 reject $\boldsymbol{\theta}'_{\text{meta}}$, and set $\boldsymbol{\theta}_{\text{meta}}^{k+1} = \boldsymbol{\theta}_{\text{meta}}^k$.
end
 - Increment the counter $k = k + 1$.
- until** Convergence criterion is satisfied.

tion between consecutive states in the Markov chain (Geman and Geman, 1984). This enables a more efficient exploration of the metaparameter space. As noted earlier, the horizontal correlation length l_h is treated discretely to facilitate the use of PCA during history matching. We treat l_h by sampling from a continuous distribution and then assigning the closest discrete value.

A Gaussian distribution centered on the current sample, $\mathcal{N}\left((\theta_{\text{meta}})_i^k, \sigma_i^2\right)$, is used as the proposal distribution, where σ_i represents the standard deviation of the proposal distribution for metaparameter i . A large standard deviation enables fast exploration of the metaparameter space at the cost of low acceptance rates (Gelman et al., 1997; Andrieu and Thoms, 2008). A small standard deviation can increase the acceptance rates but slow the exploration of the metaparameter space. This could also result in highly correlated samples and poor convergence (Gelman et al., 1997). In this study, we specify $\sigma_i = [(\theta_{\text{meta}})_{i,\text{max}} - (\theta_{\text{meta}})_{i,\text{min}}]/6$, where $(\theta_{\text{meta}})_{i,\text{max}}$ and $(\theta_{\text{meta}})_{i,\text{min}}$ are the maximum and minimum values in the prior distribution. We found this treatment to provide efficient exploration of the metaparameter space.

MCMC sampling results in the initial ‘burn-in’ period must be discarded to ensure that the initial state and transient behavior of the Markov chain do not bias the predictions. In this work, the burn-in period is taken to be 10,000 iterations, which falls within the ranges suggested by Kruschke (2014) and Fang et al. (2020) for practical applications. In addition, a convergence criterion based on the average relative change of the bin-wise posterior probability density (Nicolaidou et al., 2022) is incorporated into the sampling algorithm. The bin-wise posterior probability density refers to the posterior probability density computed on discrete bins (e.g., 10 bins in this study) or

intervals of the metaparameter values. The posterior distributions of meta-parameters are considered to be converged when the average relative change of the bin-wise posterior probability density falls below a threshold of 0.01.

5. Surrogate Model Evaluation

In this section, we first describe the geomodel and simulation setup. We then present aggregate error statistics for (new) test cases, spanning multiple geological scenarios, using the extended recurrent R-U-Net surrogate model. Detailed results for specific cases are then presented.

5.1. Geomodel and simulation setup

Some of the geomodel properties considered in this study are based on In Salah (White et al., 2014; Li and Laloui, 2016), an onshore storage project in Algeria that was active from 2004-2011. Here, however, we consider a larger overall system with much higher CO₂ injection rates, as our interest is in modeling future industrial-scale operations. More specifically, at In Salah, 3.8 Mt of CO₂ were injected over a seven-year injection period (Li and Laloui, 2016) (an average of 0.54 Mt/year), while in this study we consider injection rates of 4 Mt/year, with injection proceeding over 30 years.

As noted in Section 2, the overall system is of physical dimensions 120 km × 120 km × 100 m. The full model is represented on a grid containing 100 × 100 × 20 cells (total of 200,000 cells). The storage aquifer, located in the center of the model, is 12 km × 12 km × 100 m, which corresponds to 80 × 80 × 20 cells (128,000 cells). The cell size within the storage aquifer is constant, while cell size increases with distance from the storage aquifer in the surrounding region. This setup provides computational efficiency gains

relative to using a uniform grid over the entire $120 \text{ km} \times 120 \text{ km} \times 100 \text{ m}$ region.

As explained in Section 2, geomodels for the storage aquifer are constructed based on the metaparameters sampled from their prior distributions. The horizontal correlation length, mean and standard deviation of the log-permeability field, as well as the coefficients relating porosity and permeability, are sampled from uniform prior distributions. The permeability anisotropy ratio is sampled from a log-uniform prior distribution. The values of rock physics parameters, as well as ranges for prior distributions of the metaparameters, are presented in Table 2. Cutoff values for porosity (0.05 and 0.4) and permeability (10^{-4} md and 10^4 md) are applied to avoid non-physical values. The porosity and permeability of the domain surrounding the storage aquifer are set to 0.1 and 10 md, consistent with the average porosity and permeability of the In Salah storage aquifer (Li and Laloui, 2016).

The relative permeability and capillary pressure curves used for our flow simulations are based on measured data for Berea sandstone (Krevor et al., 2012) (the curves reported for In Salah led to numerical problems in our simulations). The CO₂-water relative permeability curves are shown in Fig. 3a. These curves correspond to Corey coefficients of $n_w = 6$, $n_g = 5$, and $k_{rg}(S_{wi}) = 0.95$, where n_w and n_g are the relative permeability exponents and $k_{rg}(S_{wi})$ is the relative permeability of CO₂ at irreducible water saturation (S_{wi}). The Brooks-Corey (Saadatpoor et al., 2010) model, with exponent (λ) of 0.67, is used to generate the capillary pressure curves. The Leverett J-function is used to provide the capillary pressure curve for each cell. The capillary pres-

Table 2: Parameters used in the flow simulations

Storage aquifer parameters	Values or ranges
Mean of log-permeability, $\mu_{\log k}$	$\mu_{\log k} \sim U(1.5, 4): (4.5, 54.6)$ md
Standard deviation of log-permeability, $\sigma_{\log k}$	$\sigma_{\log k} \sim U(1, 2.5)$
Parameter d in $\log k - \phi$ correlation	$d \sim U(0.02, 0.04)$
Parameter e in $\log k - \phi$ correlation	$e \sim U(0.05, 0.1)$
Horizontal correlation length, l_h	$l_h \in \{10, 15, 20, 25, 30\}$ cells
Vertical correlation length, l_v	2 cells
Permeability anisotropy ratio, a_r	$\log_{10}(a_r) \sim U(-2, 0)$
Surrounding region parameters	Values
Permeability	10 md
Porosity	0.1
Relative permeability and capillary pressure	Values
Irreducible water saturation, S_{wi}	0.2
Residual CO ₂ saturation, S_{gr}	0
Water exponent for Corey model, n_w	6
CO ₂ exponent for Corey model, n_g	5
Relative permeability of CO ₂ at S_{wi} , $k_{rg}(S_{wi})$	0.95
Capillary pressure exponent λ	0.67

sure curve for porosity of 0.1 and permeability of 10 md is shown in Fig. 3b.

Consistent with the conditions at In Salah, we set the initial hydrostatic pressure in the middle layer of the overall domain to 19 MPa. Temperature is constant throughout the domain at 90 °C. At initial conditions, the viscosity of the supercritical CO₂ is 0.047 cp, and the viscosity of brine is 0.38 cp. No-flow conditions are prescribed at the boundaries of the full domain. Four fully-penetrating vertical wells, denoted I1 – I4, operate within the storage aquifer. The injection well locations, along with the observation well locations (O1 – O4), are shown in Fig. 4. Each well injects 1 Mt CO₂ per year for 30 years. In the absence of a detailed well model, the injection rate into each cell intersected by the well is specified to be proportional to the well-block

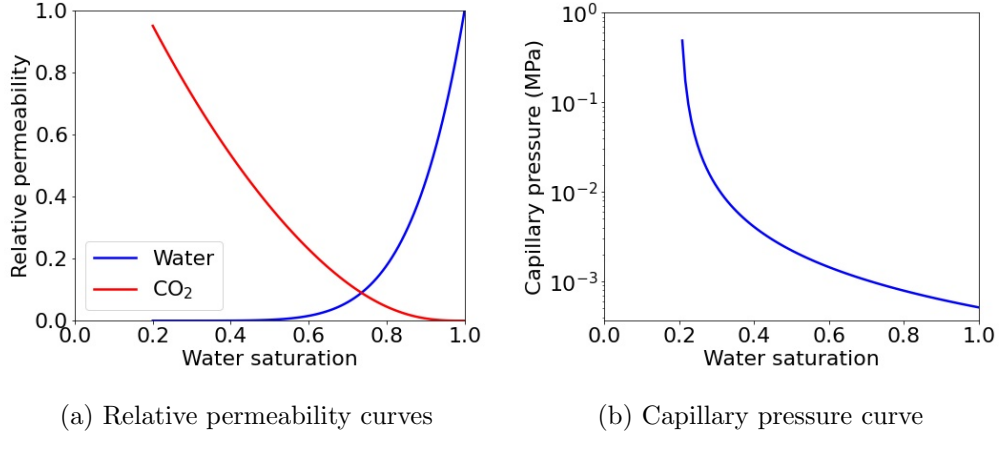


Figure 3: Two-phase flow curves. Capillary pressure curve in (b) is for $\phi = 0.1$ and $k = 10 \text{ md}$.

permeability. This treatment approximates the injection profile that would result from the use of a general well model.

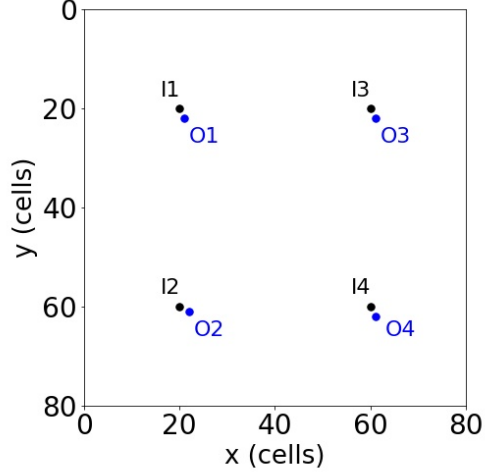


Figure 4: Locations of injection wells (I1 – I4) and observation wells (O1 – O4) in the $80 \times 80 \times 20$ storage aquifer. All wells are fully penetrating.

5.2. Surrogate model error statistics and predictions

The process for generating the training and test data is as follows. We generate 2000 standard multi-Gaussian realizations with SGeMS. The geo-model realizations are then constructed from the multi-Gaussian fields and metaparameters (sampled from their prior distributions), as described in Section 2. Flow simulation is then performed for each realization using GEOS. The pressure and saturation fields in the storage aquifer are collected at 10 discrete time steps (specifically 1.5, 3, 4.5, 7.5, 10.5, 13.5, 18, 22.5, 27 and 30 years after the start of injection). Separate surrogate models are trained for saturation and pressure. A test set of $n_e = 500$ new geomodels is then generated and simulated using the same procedures. This set is used to evaluate the performance of the surrogate model, as we now describe.

We first present error quantities for CO₂ saturation and pressure. The relative error in CO₂ saturation, for test sample i ($i = 1, \dots, 500$) is denoted δ_S^i . This is computed as

$$\delta_S^i = \frac{1}{n_s n_t} \sum_{j=1}^{n_s} \sum_{t=1}^{n_t} \frac{|(\hat{S}_s)_{i,j}^t - (S_s)_{i,j}^t|}{(S_s)_{i,j}^t + \epsilon}, \quad (12)$$

where $n_s = 128,000$ is the total number of cells in the storage aquifer, $n_t = 10$ is the number of output time steps considered, and $(S_s)_{i,j}^t$ and $(\hat{S}_s)_{i,j}^t$ are CO₂ saturation predictions from GEOS and the surrogate model, respectively, for test case i , cell j and time step t . A constant $\epsilon = 0.025$ is included to prevent division by zero (or a very small value).

The relative error for pressure for sample i ($i = 1, \dots, 500$), denoted δ_p^i , is defined similarly, though in this case we normalize by the difference between the maximum and minimum pressure, i.e.,

$$\delta_p^i = \frac{1}{n_s n_t} \sum_{j=1}^{n_s} \sum_{t=1}^{n_t} \frac{|(\hat{p}_s)_{i,j}^t - (p_s)_{i,j}^t|}{(p_s)_{i,\max}^t - (p_s)_{i,\min}^t}. \quad (13)$$

Here $(p_s)_{i,j}^t$ and $(\hat{p}_s)_{i,j}^t$ are pressure predictions from GEOS and the surrogate model, for test case i , cell j and time step t , and $(p_s)_{i,\max}^t$ and $(p_s)_{i,\min}^t$ are the maximum and minimum pressure for all cells in test case i at time step t .

Histograms of the test-case relative errors for saturation and pressure are displayed in Fig. 5. The mean and median relative errors for saturation over the 500 test cases are 5.4% and 4.5%, respectively, and for pressure they are 1.9% and 1.3%. These errors are comparable to (but slightly larger than) those achieved in Tang et al. (2022a), where average saturation and pressure errors of 5.3% and 0.3% were reported for test cases drawn from a single geological scenario. In the saturation error calculation in Tang et al. (2022a), $\epsilon = 0.01$ was used, which would tend to inflate the errors in that study compared to those reported here. In any event, the small relative errors achieved here demonstrate the applicability of the surrogate model for geomodels drawn from a wide range of geological scenarios.

We next present detailed results for the case corresponding to the median relative saturation error. The geomodel for this case is shown in Fig. 6. This realization corresponds to the following metaparameters: horizontal correlation length of 1500 m, $\mu_{\log k}$ of 2.27, $\sigma_{\log k}$ of 2.06, permeability anisotropy ratio of 0.4, and d and e values of 0.03 and 0.05. The saturation and pressure fields for this test case at 4.5, 13.5, and 30 years are displayed in Figs. 7 and 8. The upper rows in the figures show the reference GEOS results, while the

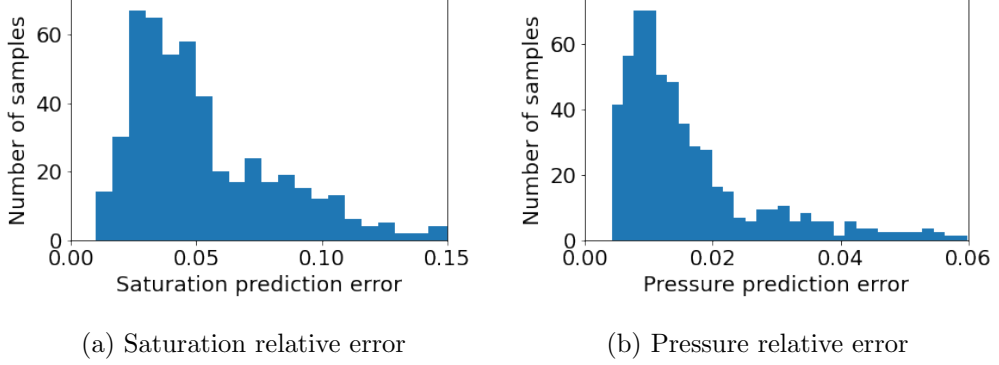


Figure 5: Histograms of relative errors for the 500 test cases.

lower rows display the surrogate model results. There is close visual correspondence between the flow simulation and surrogate model results for both quantities. The saturation plumes display irregular shapes (most notably at 30 years) due to the highly heterogeneous porosity and log-permeability fields. The plume radii at the end of injection are larger in the upper layers than the lower layers due to the relatively high permeability anisotropy ratio.

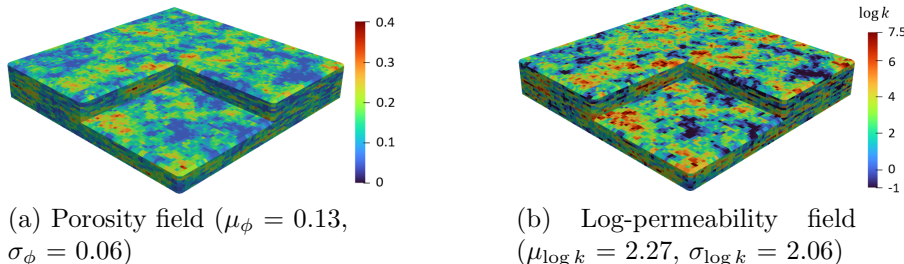


Figure 6: Porosity and log-permeability fields of test-case realization corresponding to median relative saturation error.

The pressure fields for the same test case are shown in Fig. 8. The surrogate predictions are again very close to the GEOS results. At early time, pressure buildup is mainly around the injection wells (Fig. 8a and d).

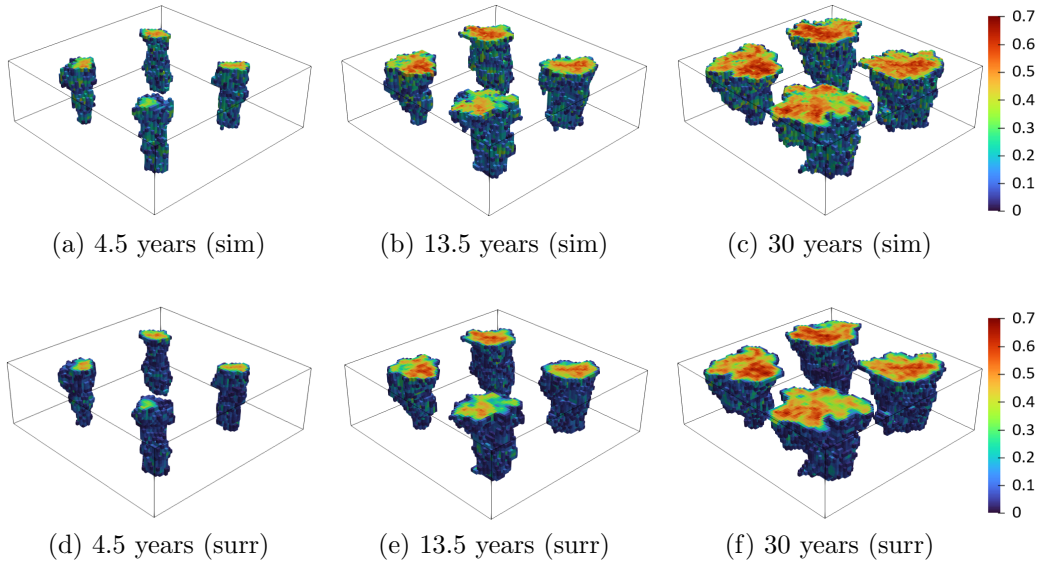


Figure 7: CO₂ saturation in the storage aquifer from GEOS flow simulation (upper row) and the extended recurrent R-U-Net surrogate model (lower row) for representative test case at three time steps.

The no-flow boundaries, although distant, eventually impact the pressure field. This is evident in the significantly increased pressure, over the full storage aquifer, after 30 years (Fig. 8c and f).

5.3. Surrogate predictions for geomodels from various scenarios

The saturation plumes and pressure fields for geomodel realizations drawn from different geological scenarios can vary substantially. Vertical permeability, for example, impacts vertical CO₂ migration, which is driven by gravity and density difference (the density of supercritical CO₂ and brine are 610 kg/m³ and 975 kg/m³, respectively, at initial conditions). The anisotropy ratio can therefore have a significant effect on the shape and extent of the plume. In addition, mean porosity and mean log-permeability can have large

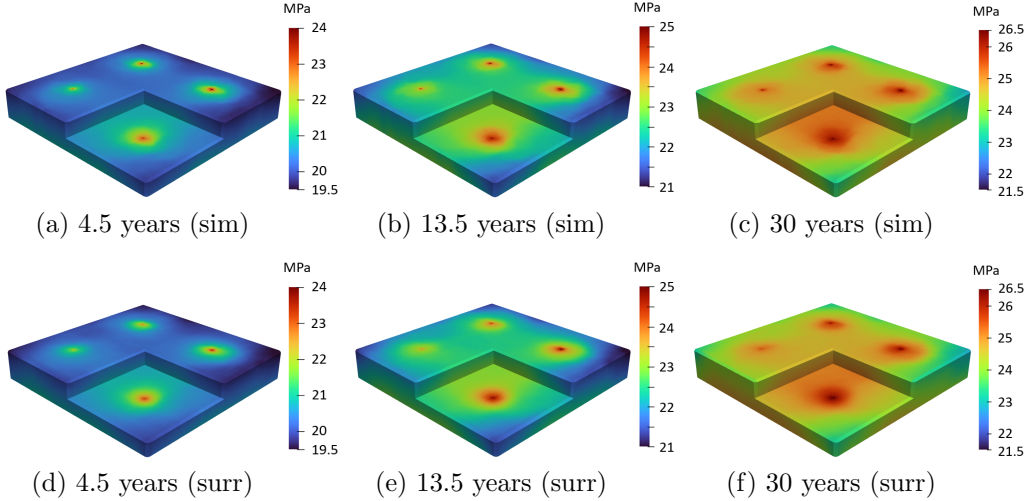
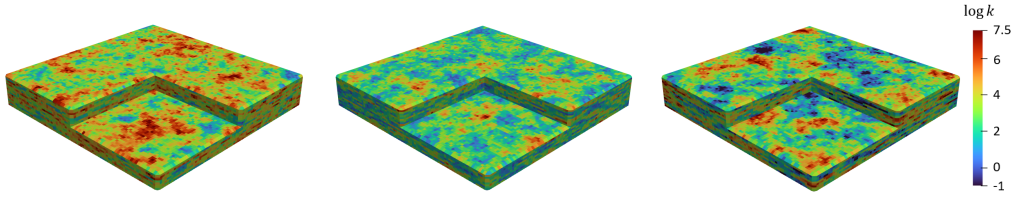


Figure 8: Pressure in the storage aquifer from GEOS flow simulation (upper row) and the extended recurrent R-U-Net surrogate model (lower row) for representative test case at three time steps.

impacts on the pressure field. These quantities all correspond to metaparameters that vary over substantial ranges in this study.

We thus consider saturation and pressure predictions for geomodels drawn from scenarios characterized by different metaparameter values. The log-permeability fields for three realizations, each from a different geological scenario, are displayed in Fig. 9. The realizations vary significantly in appearance, and they also vary in $a_r = k_v/k$, which is not evident in the figure because $\log k$ is the quantity displayed.

The CO₂ saturation plumes at the end of injection for these three geomodels are shown in Fig. 10. The relative saturation errors are 1.6%, 6.1% and 3.3%, respectively. Of particular interest here is the general agreement between the GEOS and surrogate model results, which requires the surrogate model to capture a range of plume shapes and extents. For Realization 1,



(a) Realization 1 ($\mu_{\log k} = 3.78$, $\sigma_{\log k} = 1.42$, $a_r = 0.56$) (b) Realization 2 ($\mu_{\log k} = 2.44$, $\sigma_{\log k} = 1.37$, $a_r = 0.14$) (c) Realization 3 ($\mu_{\log k} = 2.92$, $\sigma_{\log k} = 1.77$, $a_r = 0.01$)

Figure 9: Log-permeability ($\log k$) fields for geomodels drawn from three geological scenarios. Geomodels in (a) and (b) are the ‘true’ log-permeability fields used for history matching in Section 6.

$a_r = 0.56$. With this relatively large anisotropy ratio vertical flow is not impeded, leading to conical-shaped saturation plumes (Fig. 10a and d). Because CO₂ migrates vertically due to gravity effects, the plume radii in the top layer of the model are large. For Realizations 2 and 3, $a_r = 0.14$ and 0.01, respectively. Vertical flow is thus more restricted, and the plume shapes shift from conical (Fig. 10a and d) to cylindrical (Fig. 10b and e) to irregular (Fig. 10c and f). As a result of geological heterogeneity, the saturation plumes associated with the four injection wells display clear differences in all cases. Importantly, these effects are captured by the surrogate model.

The pressure fields at the end of the injection period for these geomodels are shown in Fig. 11. The correspondence between surrogate model and GEOS results is again very close despite the variation in solution character. The surrogate model relative pressure errors for Realizations 1, 2 and 3 are 1.3%, 2.2% and 1.0%, respectively. The highest pressure buildup is observed in Realization 2, which is reasonable because this model corresponds to the lowest $\mu_{\log k}$ (2.44). The pressure fields for Realizations 1 and 3 are different in character, which could be due to the different metaparameters and/or to

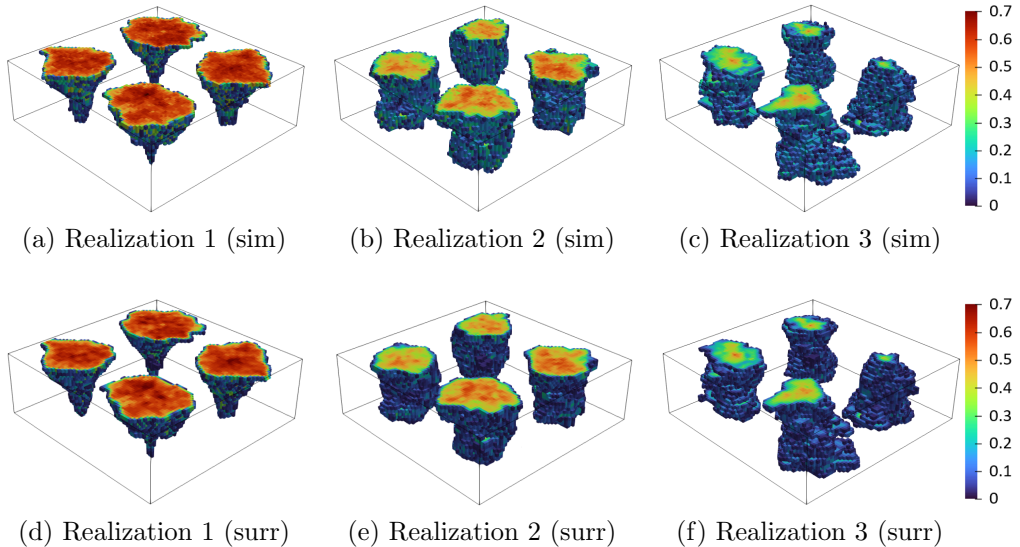


Figure 10: CO₂ saturation in the storage aquifer after 30 years of injection from GEOS (upper row) and the surrogate model (lower row) for geomodels drawn from three geological scenarios. Corresponding geological realizations shown in Fig. 9.

differences in near-well properties, with Realization 1 showing a more uniform response.

As noted earlier, vertical observation wells (denoted O1 – O4), shown in Fig. 4, are positioned near each of the four injection wells. These observation wells provide the saturation and pressure data that will be used in history matching. To evaluate the accuracy of surrogate model predictions for this type of data, we now assess the overall (statistical) correspondence between GEOS and surrogate model results for monitoring well data. Specifically, we consider P₁₀, P₅₀ and P₉₀ (10th, 50th and 90th percentile) results, for both saturation and pressure, at particular locations through time.

The ensemble statistical results (P₁₀, P₅₀ and P₉₀ curves) for saturation and pressure are shown in Figs. 12 and 13. The solid black curves represent

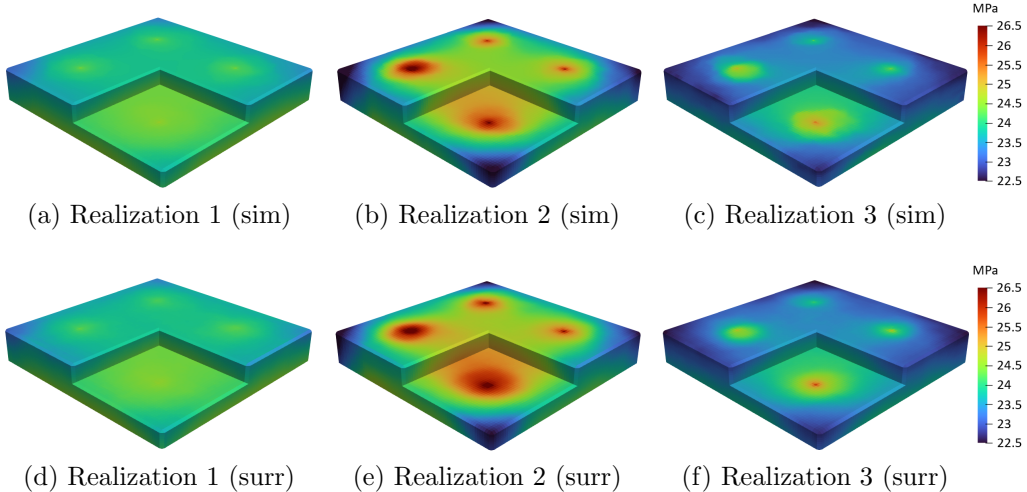


Figure 11: Pressure fields in the storage aquifer after 30 years of injection from GEOS (upper row) and the surrogate model (lower row) for geomodels drawn from three geological scenarios. Corresponding geological realizations shown in Fig. 9.

GEOS results, and the dashed red curves are surrogate model results. The upper curves are the P_{90} results (at each of the 10 time steps), the middle curves are the P_{50} results, and the lower curves the P_{10} results. Although each monitoring well can provide data at all 20 layers, the results presented are for one particular layer. Close agreement is consistently observed between the two sets of results, indicating that, at least in a statistical sense, the surrogate model is able to provide accurate predictions at specific monitoring well locations. This capability is essential for history matching.

There are noticeable differences in the P_{10} – P_{90} ranges for saturation in the top (Fig. 12a) and bottom (Fig. 12d) layers. This is due to gravity effects, which drive CO₂ upward. The clear increase in pressure with time, which results in large part from the no-flow outer boundary conditions, is evident in Fig. 13. The change in pressure with time (dp/dt) becomes essentially

constant, in space and time, after several years of injection. This is a characteristic of the pseudo-steady state flow regime, which is expected given the problem setup.

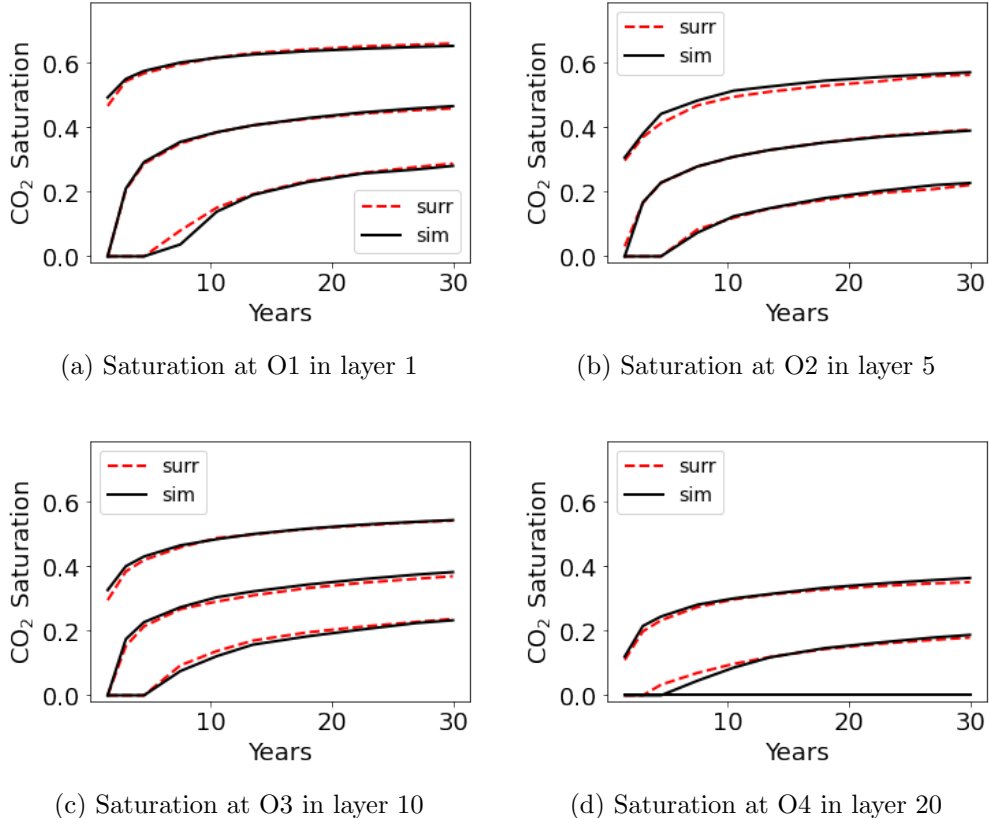


Figure 12: Saturation ensemble statistics from GEOS (black solid curves) and surrogate model (red dashed curves) at four observation locations. The upper, middle and lower curves correspond to P₁₀, P₅₀ and P₉₀ results over the full ensemble of 500 test cases.

6. History Matching using Surrogate Model

We now apply the MCMC-based history matching procedure in combination with the extended recurrent R-U-Net surrogate model to estimate the

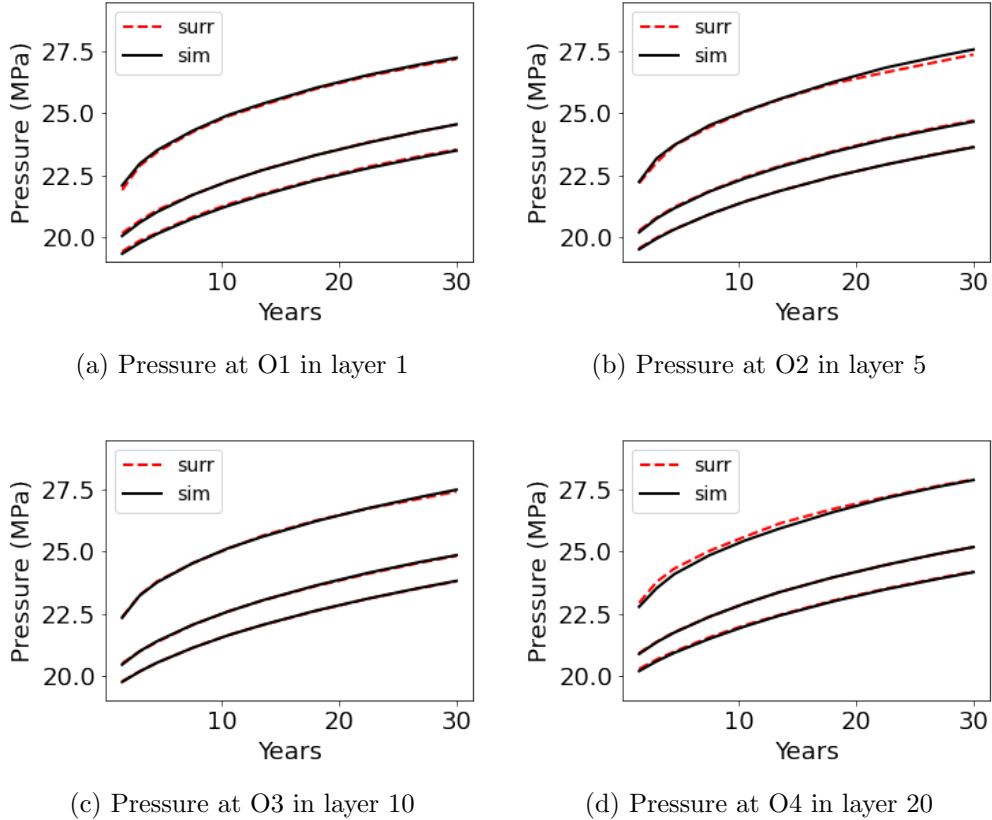


Figure 13: Pressure ensemble statistics from GEOS (black solid curves) and surrogate model (red dashed curves) at four observation locations. The upper, middle and lower curves correspond to P_{10} , P_{50} and P_{90} results over the full ensemble of 500 test cases.

posterior distributions of the six metaparameters. Saturation and pressure measurements in the monitoring wells provide the observed data. We first describe the setup for the history matching problem, including our treatment of error, and then present history matching results for two new (random) synthetic ‘true’ models.

6.1. Problem setup for history matching

The synthetic true models, denoted \mathbf{m}_{true} , correspond to newly generated samples from the (broad) prior distribution. Specifically, the metaparameters are first sampled, and then a particular realization is drawn. The log-permeability fields of the two true models are shown in Fig. 9a and b. The models are considered one at a time. Flow simulation is performed on the true model, and these simulation results, at observation-well locations, are taken as true data, denoted by \mathbf{d}_{true} . The observed data used in history matching, denoted \mathbf{d}_{obs} , are obtained by adding random error to \mathbf{d}_{true} .

In this study, the error considered in the history matching workflow includes measurement error, model-resolution error, and surrogate-model error. The measurement error derives from the actual measurements of pressure and (interpreted) saturation-log values. Resolution error, which can also be viewed as upscaling error, arises from the mismatch between model resolution (grid cells are of dimensions 150 m \times 150 m \times 5 m) and the scale of the measured data (cm to m). Surrogate model error arises because we use the surrogate model, rather than the reference simulator GEOS, to provide flow predictions for the MCMC procedure.

The observed data are measured at three time steps (1.5 years, 3 years, 4.5 years) after the start of injection. The observed saturation data include measurements, taken at layers 1, 10 and 20, in each of the four observation wells (resulting in a total of 36 saturation measurements). Pressure data are measured at layer 1 in each of the observation wells, leading to a total of 12 pressure measurements. The observed data, with measurement error and

model-resolution error, is expressed as

$$\mathbf{d}_{\text{obs}} = \mathbf{d}_{\text{true}} + \boldsymbol{\epsilon} = f(\mathbf{m}_{\text{true}}) + \boldsymbol{\epsilon}, \quad (14)$$

where $f(\mathbf{m}_{\text{true}})$ represents flow simulation results for the true model \mathbf{m}_{true} , and $\boldsymbol{\epsilon}$ denotes the measurement and model-resolution error. This quantity, which is taken to be normally distributed and uncorrelated, is sampled with $\mathbf{0}$ mean and covariance \tilde{C}_D . This covariance involves two contributions, i.e., $\tilde{C}_D = C_D + C_{\text{res}}$, where C_D is the measurement error covariance and C_{res} is the covariance associated with model resolution.

Measurement error derives from the measurement device and data interpretation, and these can be readily quantified/estimated. Model resolution error, which is typically much larger than measurement error, is more difficult to assess. This error includes grid resolution and subgrid heterogeneity effects, though other modeling treatments and approximations, such as those associated with relative permeability, capillary pressure, hysteresis, dissolution functions, etc., also contribute and should be considered. Our approach here is relatively simple. From a limited grid resolution study, we found the standard deviation of the (combined) measurement and resolution errors to be around 0.1 (saturation units) for saturation, and 0.1 MPa for pressure. This pressure error corresponds to that used by Sun and Durlofsky (2019), though the saturation error is larger. We considered a few different values (over a reasonable range) for these error parameters and did not observe significant differences in MCMC results. Accurate quantification of resolution/model error may be important in some settings and should be considered in future work.

The surrogate modeling error is more straightforward to estimate. This error, denoted ϵ_{surr} , can be expressed as

$$\epsilon_{\text{surr}} = f(\mathbf{m}_{\text{true}}) - \hat{f}(\mathbf{m}_{\text{true}}), \quad (15)$$

where $f(\mathbf{m}_{\text{true}})$ and $\hat{f}(\mathbf{m}_{\text{true}})$ represent the GEOS and surrogate model predictions for saturation or pressure (for the true model). Based on our evaluation of the test set, we found the surrogate model error to be unbiased. The standard deviation of the surrogate model error for saturation was 0.05, and that for pressure was 0.14 MPa (these estimates are over the full ensemble of 500 test cases).

As discussed in Section 4, surrogate predictions $\hat{f}(\mathbf{m}_s)$ for new geomodels, constructed based on the proposed metaparameters, are used in the likelihood computation. The likelihood function is expressed as

$$p(\mathbf{d}_{\text{obs}} | \boldsymbol{\theta}_{\text{meta}}) = c \exp \left(-\frac{1}{2} \left(\mathbf{d}_{\text{obs}} - \hat{f}(\mathbf{m}_s) \right)^T C_{\text{tot}}^{-1} \left(\mathbf{d}_{\text{obs}} - \hat{f}(\mathbf{m}_s) \right) \right), \quad (16)$$

where c is a normalization constant and C_{tot} is the total covariance, given by

$$C_{\text{tot}} = \tilde{C}_{\text{D}} + C_{\text{surr}}. \quad (17)$$

Here C_{surr} represents the covariance of the surrogate model error. The errors discussed above were quantified in terms of standard deviation. For pressure, the corresponding C_{tot} is $C_{\text{tot}} = [(0.1)^2 + (0.14)^2] = 0.0296$ (all terms in units of MPa). For saturation we have $C_{\text{tot}} = [(0.1)^2 + (0.05)^2] = 0.0125$.

6.2. History matching results for true model 1

For true model 1 (shown in Fig. 9a), the MCMC history matching procedure requires about 4,381,000 function evaluations to achieve convergence in the posterior distributions of the metaparameters. Only about 16,700 of the proposed models (metaparameters and the corresponding geomodel realizations) are accepted, which corresponds to an acceptance rate of about 0.4%. Each surrogate model evaluation for saturation and pressure requires approximately 0.15 seconds on a single Nvidia Tesla V100 GPU. The high-fidelity (GEOS) flow simulations require about 5 minutes per run using 64 AMD EPYC-7543 CPU cores in parallel. Although the hardware environments for the two approaches are quite different, we achieve a speedup factor of 2000 in elapsed time with the surrogate model. Given the sequential nature of the MCMC procedure, the elapsed time for history matching with the surrogate model is about 1 week. Execution of this procedure would not be possible using high-fidelity flow simulation.

History matching results for the metaparameters for this case are displayed in Fig. 14. The grey regions indicate the prior distributions (which are uniform), the blue histograms represent the posterior distributions, and the red vertical dashed lines display the true values. The true values consistently fall within the posterior distributions. Substantial uncertainty reduction in the mean of the log-permeability field and in the permeability anisotropy ratio is clearly achieved (Fig. 14a and b). A degree of uncertainty reduction is observed in permeability standard deviation, horizontal correlation length, and the parameter d (Fig. 14c, d and e). The parameter e , however, is underestimated.

Recall that d and e relate porosity and permeability via an equation of the form $\phi = d \cdot \log k + e$ (Eq. 4). It is thus instructive to consider the prior and posterior distributions for porosity directly. These are displayed in Fig. 14g and h. It is evident that, although history matching does not provide significant uncertainty reduction for d and e individually, it does reduce uncertainty in the mean (μ_ϕ) and standard deviation (σ_ϕ) of porosity. Thus we conclude that it is these values, rather than the cell-by-cell relationship between porosity and permeability, for which the measured data are informative.

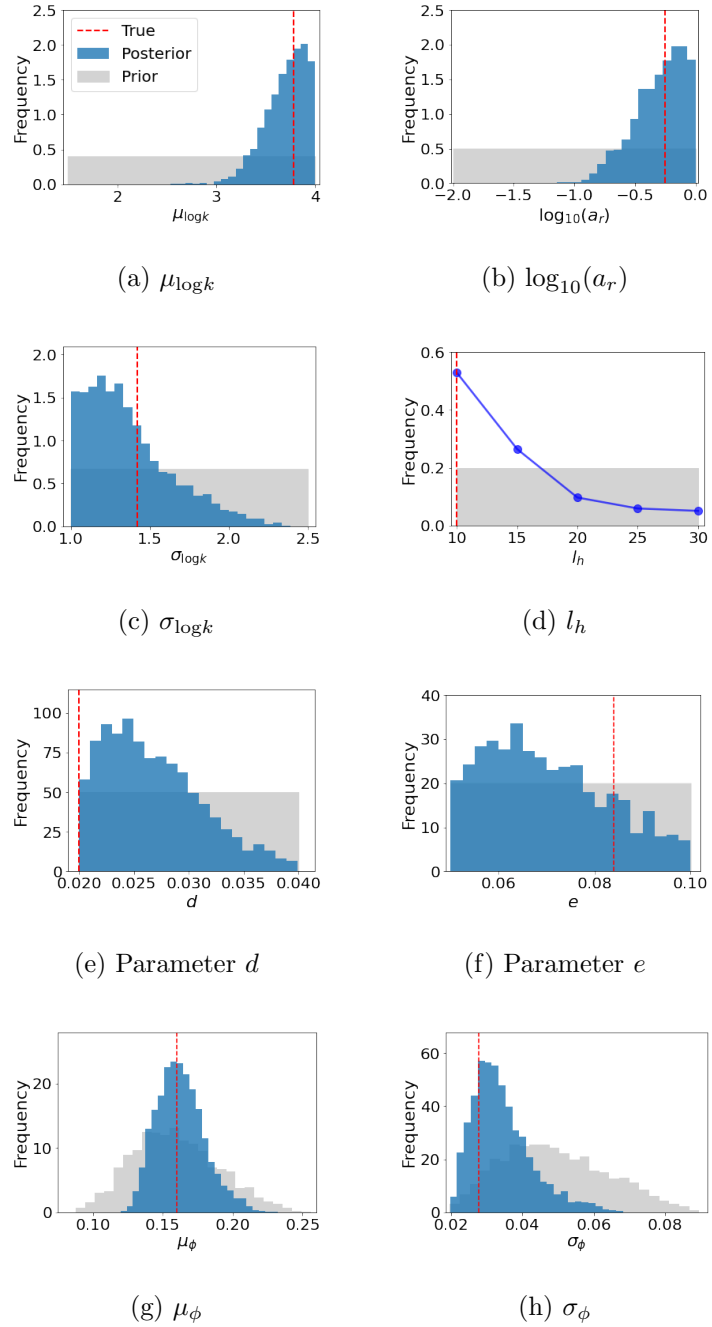


Figure 14: History matching results for the metaparameters for true model 1. Gray regions represent prior distributions, blue histograms are posterior distributions, and red vertical lines denote true values. Legend in (a) applies to all subplots.

History matching results for saturation and pressure at four observation locations are shown in Figs. 15 and 16. In these figures, the grey regions represent the prior P_{10} – P_{90} range, the red curves display the true data (simulation results without any error), and the red circles denote the observed data (which includes measurement and resolution error). The blue solid curves represent the P_{50} posterior results, while the blue dashed curves show the P_{10} (lower) and P_{90} (upper) posterior results. Significant uncertainty reduction in saturation is achieved at the top and bottom layers of the storage aquifer in Fig. 15, though very little uncertainty reduction is observed in layer 5 (where no measurements are made). Pressure at all four observation locations, at different depths, exhibits substantial uncertainty reduction (Fig. 16). This indicates that the pressure measurements, though limited, are highly informative in terms of pressure at monitoring well locations.

The shape and extent of the CO₂ saturation plumes, and the pressure fields within the storage aquifer, are of particular interest. We now display saturation plumes and pressure fields, after 30 years of injection, corresponding to prior and posterior models. Our approach for finding representative samples of these prior and posterior solutions is as follows. We first select, randomly, a total of 1000 prior geomodels (out of the 2000 geomodels used for training) and 1000 posterior geomodels (out of the 16,700 posterior geomodels accepted by MCMC). The saturation and pressure fields for these prior and posterior geomodels (at 30 years) are then generated using the surrogate model. We then apply a k-means clustering method to provide five clusters for each case. Finally, a k-medoids method is used to identify the ‘center’ of each cluster. These five prior and five posterior (cluster center) solutions can

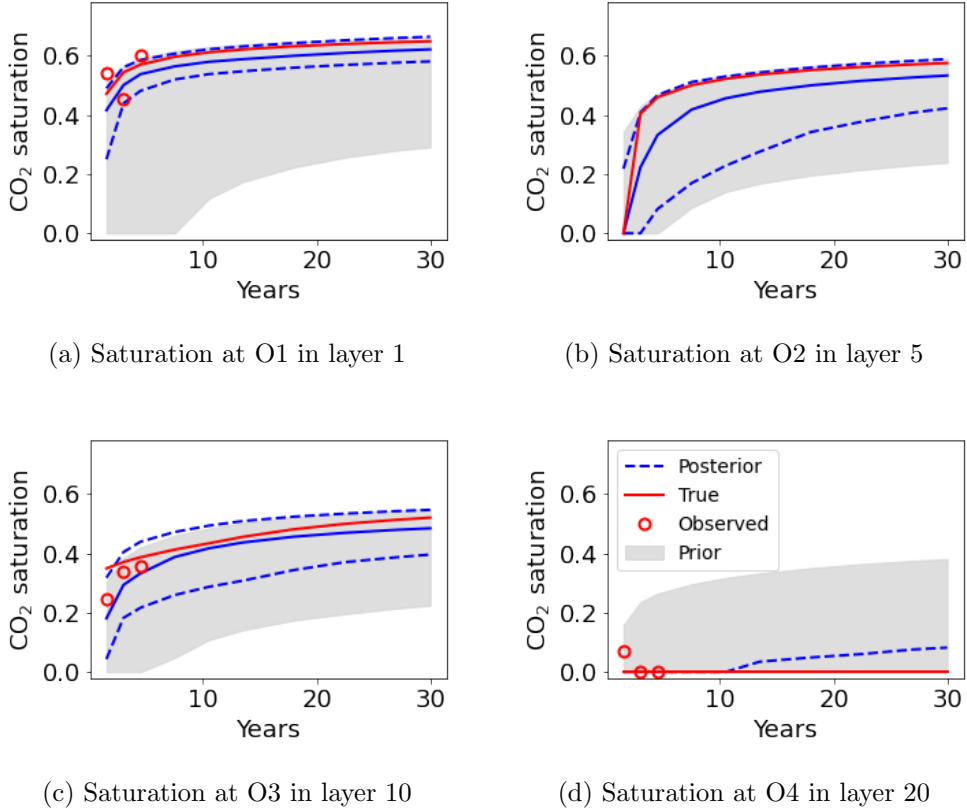


Figure 15: History matching results for saturation at four observation locations for true model 1. Grey regions represent the prior $P_{10}-P_{90}$ range, red circles and red lines denote observed and true data, and blue curves show the posterior P_{10} , P_{50} and P_{90} predictions from the surrogate model. Legend in (d) applies to all subplots.

be viewed as representative saturation and pressure fields.

The resulting prior and posterior saturation fields, at 30 years, are shown in Fig. 17. A high degree of variability, with significant differences in the shape and extent of the saturation plumes, is observed in the priors (top row). This is consistent with the variability shown earlier in Fig. 10. The prior plume geometries vary from conical to cylindrical to irregular as we

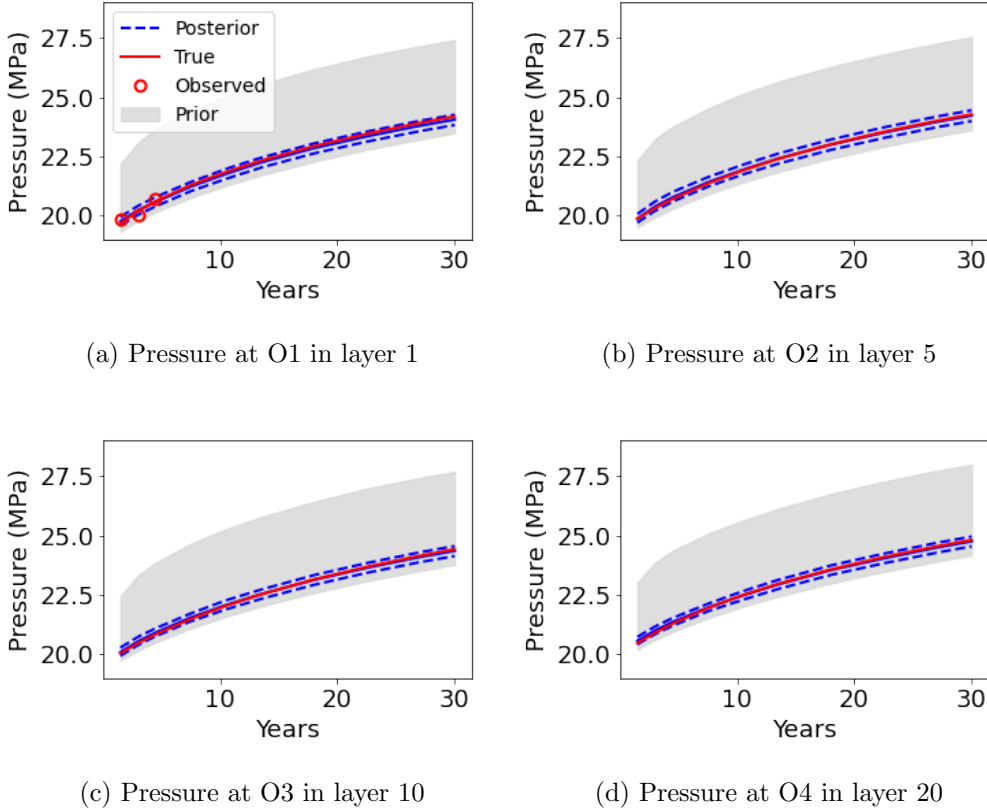


Figure 16: History matching results for pressure at four observation locations for true model 1. Grey regions represent the prior P_{10} – P_{90} range, red circles and red lines denote observed and true data, and blue curves show the posterior P_{10} , P_{50} and P_{90} predictions from the surrogate model. Note that pressure data for history matching are only measured in layer 1. Legend in (a) applies to all subplots.

proceed from Fig. 17a to e. The plume corresponding to true model 1 is shown in Fig. 10a. The plumes for the posterior geomodels (lower row of Fig. 17) show much less variability than those for the prior geomodels, and they are relatively close to the true solution. This clearly illustrates the uncertainty reduction in plume geometry provided by our MCMC-based history matching procedure.

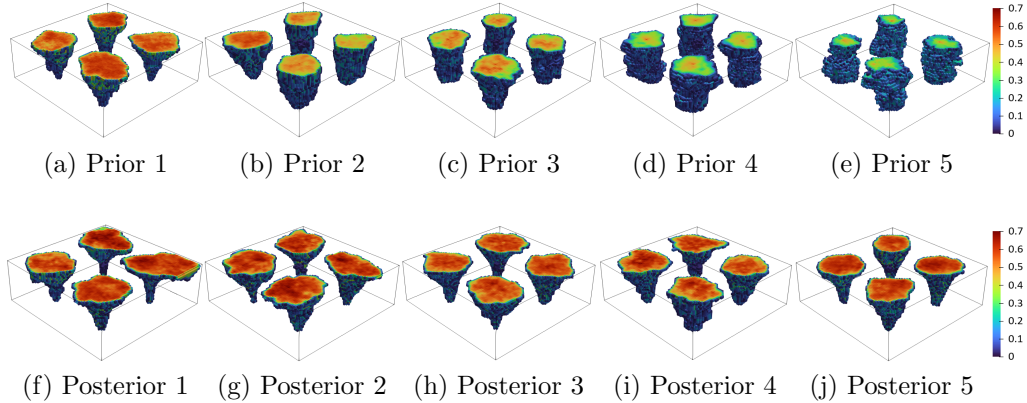


Figure 17: Representative saturation plumes for prior geomodels (upper row) and posterior geomodels (lower row), for true model 1 at 30 years. True saturation field for this case shown in Fig. 10a.

Analogous prior and posterior pressure solutions are shown in Fig. 18. The true (simulated) pressure field for this case at 30 years is shown in Fig. 11a. Again, we see a high degree of variability in the prior results (upper row of Fig. 18), which is reduced considerably in the posterior results (lower row of Fig. 18). The posterior pressure fields clearly resemble the true solution, again demonstrating the capabilities of the overall MCMC-based history matching procedure.

6.3. History matching results for true model 2

Our discussion of the true model 2 history matching results will be more limited, since these results are generally consistent with those for true model 1. True model 2 is shown in Fig. 9b. For this case the MCMC procedure required about 5,537,000 function evaluations to achieve convergence. About 14,200 geomodels (metaparameters and corresponding realizations) were accepted during history matching.

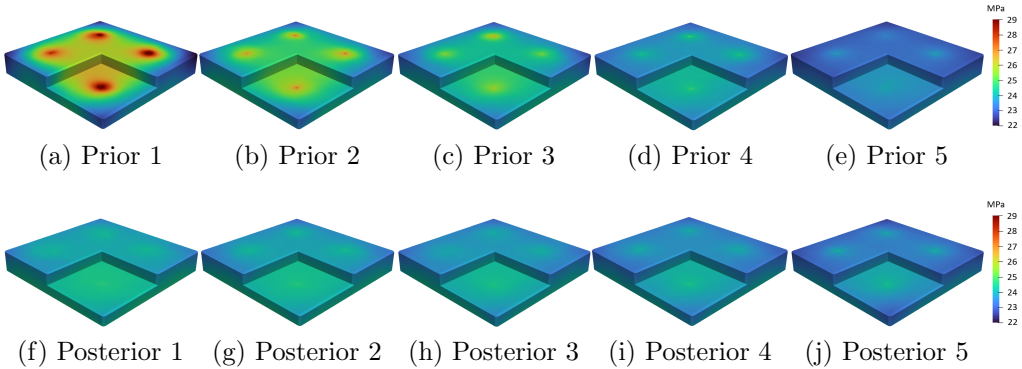


Figure 18: Representative pressure fields for prior geomodels (upper row) and posterior geomodels (lower row), for true model 1 at 30 years. True pressure field for this case shown in Fig. 11a.

Prior and posterior results for the metaparameters are shown in Fig. 19. We again observe uncertainty reduction in the key metaparameters. Approximate agreement between the true values and the peaks of the posterior distributions is achieved for permeability anisotropy ratio and log-permeability standard deviation. The mean of log-permeability is slightly overestimated. There is again little uncertainty reduction in parameters d and e individually. The mean and standard deviation of porosity are relatively accurate, though they are both slightly overestimated in this case.

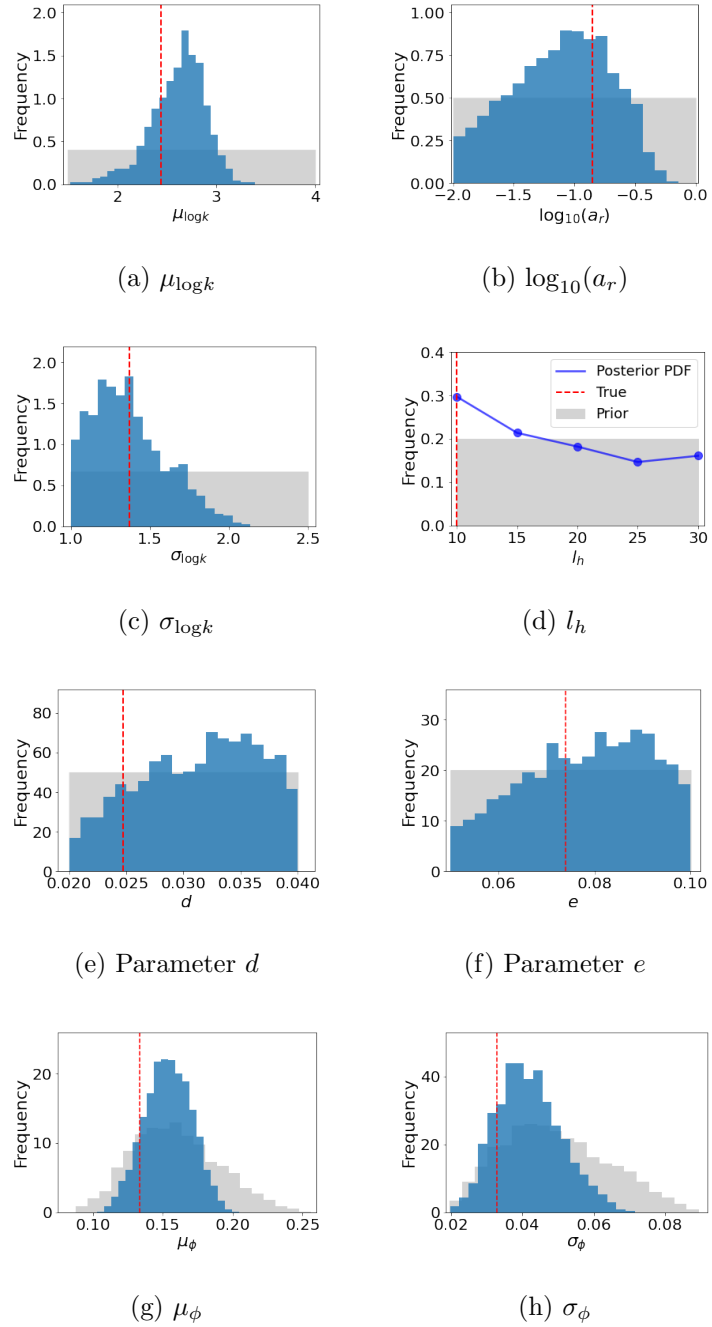


Figure 19: History matching results for the metaparameters for true model 2. Gray regions represent prior distributions, blue histograms are posterior distributions, and red vertical lines denote true values. Legend in (d) applies to all subplots.

Representative prior and posterior saturation and pressure fields are shown in Figs. 20 and 21. The true (simulated) saturation field for this case, shown in Fig. 10b, exhibits near-cylindrical plumes around all four injectors. The posterior saturation fields generally display this geometry (this is particularly evident in Fig. 20g, h and i). Consistent with our observations for true model 1, there is much less variability in the posterior saturation plumes than in the priors. Similar observations apply to the pressure fields in Fig. 21. These solutions again show reasonable agreement with the true model 2 pressure field shown in Fig. 11b (note the scales differ between Figs. 11 and 21).

It is clear from the results for both true models that substantial uncertainty reduction can be achieved by history matching to monitoring well data. The amount of uncertainty reduction actually achieved in any particular case will of course depend on the amount, type and quality (quantified in terms of error) of observations collected.

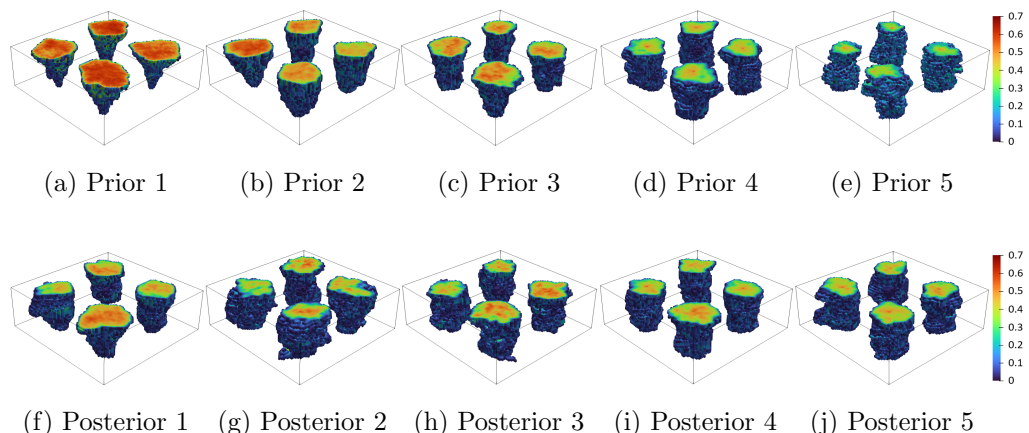


Figure 20: Representative saturation plumes for prior geomodels (upper row) and posterior geomodels (lower row), for true model 2 at 30 years. True saturation field for this case shown in Fig. 10b.

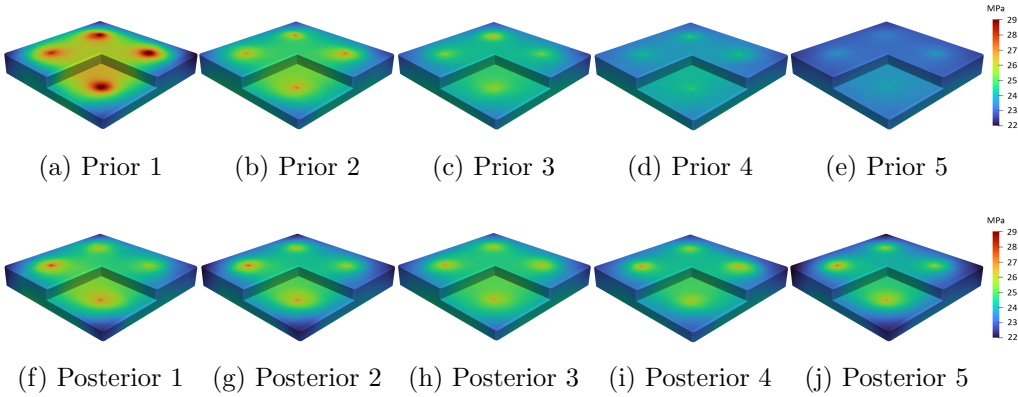


Figure 21: Representative pressure fields for prior geomodels (upper row) and posterior geomodels (lower row), for true model 2 at 30 years. True pressure field for this case shown in Fig. 11b.

7. Concluding Remarks

In this study, we extended the 3D recurrent R-U-Net surrogate model to handle geomodel realizations drawn from different geological scenarios. These scenarios are characterized by metaparameters, which in realistic cases are themselves uncertain. The metaparameters considered here are the mean and standard deviation of log-permeability, permeability anisotropy ratio, horizontal correlation length, and two parameters in the porosity – permeability relationship. For any combination of metaparameters, an infinite number of realizations can be generated. To accommodate this wide range of potential geomodels, the recurrent R-U-Net model was extended to include additional input channels. The GEOS flow simulator provided training data for the surrogate model. This training data comprised flow simulation results for 2000 random realizations, which were themselves characterized by different combinations of the six metaparameters. A history matching workflow based on a Markov chain Monte Carlo procedure was introduced to treat systems

in which the geological scenario is uncertain.

The flow setup involved a large-scale storage operation with injection of 4 Mt CO₂ per year, for 30 years, through four vertical wells. Surrogate model performance was assessed through error statistics and results for particular cases. For a set of 500 new (random) test cases, the surrogate model provided results with a median relative saturation error of 4.5% and a median relative pressure error of 1.3%. The ability of the model to provide accurate saturation and pressure predictions for geomodels from different geological scenarios was clearly demonstrated, as was the accuracy of the solutions at monitoring-well locations.

History matching results were presented for two different synthetic true models. The error considered in the history matching workflow included measurement error, model-resolution error, and surrogate-model error. The MCMC procedure required around 5,000,000 function evaluations to achieve convergence in the posterior distributions of the metaparameters. These computations are manageable using the surrogate model (which required 0.15 seconds per run on a Nvidia Tesla V100 GPU), but they would not be feasible using high-fidelity flow simulation. Uncertainty reduction in key metaparameters using the MCMC-based procedure was demonstrated for both true models. The resulting saturation plumes and pressure fields were shown to match the true model results more closely than the prior simulations.

There are a number of topics that should be considered in future research in this area. The current workflow can be extended to treat coupled flow and geomechanics problems in cases with uncertain metaparameters, including those associated with geomechanical properties such as Young's modulus. A

multiphysics surrogate modeling framework could significantly accelerate the simulations and training required for coupled problems, and this should be investigated. It will also be of interest to assess the impact of different types and quality of observed data on posterior uncertainty. This will require appropriate error models, which will need to characterize a range of modeling and resolution errors. Finally, the application of the workflow developed in this study to realistic cases should be pursued.

CRediT authorship contribution statement

Yifu Han: Conceptualization, Methodology, Software, Visualization, Formal analysis, Writing – original draft. **François P. Hamon:** GEOS software – Coding and use. **Su Jiang:** Conceptualization, Software, Writing – original draft. **Louis J. Durlofsky:** Supervision, Conceptualization, Resources, Formal analysis, Writing – review & editing.

Declaration of competing interest

The authors declare that they have no known competing financial interests or personal relationships that could have appeared to influence the work reported in this paper.

Data availability

The code used in this study will be made available on github when this paper is published. Please contact Yifu Han (yifu@stanford.edu) for earlier access.

Acknowledgements

We are grateful to the Stanford Center for Carbon Storage, Stanford Smart Fields Consortium, and TotalEnergies (through the FC-MAELSTROM project) for funding. We thank the Stanford Center for Computational Earth & Environmental Science for providing the computational resources used in this work. We also acknowledge timely assistance from GEOS developers at Lawrence Livermore National Laboratory, Stanford University, and TotalEnergies.

References

- Andrieu, C., Thoms, J., 2008. A tutorial on adaptive MCMC. *Stat. Comput.* 18, 343–373.
- Bui, Q.M., Hamon, F.P., Castelletto, N., Osei-Kuffuor, D., Settgast, R.R., White, J.A., 2021. Multigrid reduction preconditioning framework for coupled processes in porous and fractured media. *Comput. Methods Appl. Mech. Eng.* 387, 114111.
- Chen, B., Harp, D.R., Lu, Z., Pawar, R.J., 2020. Reducing uncertainty in geologic CO₂ sequestration risk assessment by assimilating monitoring data. *Int. J. Greenh. Gas Control.* 94, 102926.
- Fang, Z., Fang, H., Demanet, L., 2020. Deep generator priors for Bayesian seismic inversion. *Adv. Geophys.* 61, 179–216.
- Gelman, A., Gilks, W.R., Roberts, G.O., 1997. Weak convergence and opti-

- mal scaling of random walk Metropolis algorithms. *Ann. Appl. Probab.* 7, 110–120.
- Geman, S., Geman, D., 1984. Stochastic relaxation, Gibbs distributions, and the Bayesian restoration of images. *IEEE Trans. Pattern Anal. Mach. Intell.* 6, 721–741.
- González-Nicolás, A., Baù, D., Alzraiee, A., 2015. Detection of potential leakage pathways from geological carbon storage by fluid pressure data assimilation. *Adv. Water Resour.* 86, 366–384.
- Hastings, W.K., 1970. Monte Carlo sampling methods using Markov chains and their applications. *Biometrika*. 57, 97–109.
- Jahandideh, A., Hakim-Elahi, S., Jafarpour, B., 2021. Inference of rock flow and mechanical properties from injection-induced microseismic events during geologic CO₂ storage. *Int. J. Greenh. Gas Control.* 105, 103206.
- Jiang, S., Durlofsky, L.J., 2023. Use of multifidelity training data and transfer learning for efficient construction of subsurface flow surrogate models. *J. Comput. Phys.* 474, 111800.
- Jung, Y., Zhou, Q., Birkholzer, J.T., 2015. On the detection of leakage pathways in geological CO₂ storage systems using pressure monitoring data: Impact of model parameter uncertainties. *Adv. Water Resour.* 84, 112–124.
- Krevor, S.C., Pini, R., Zuo, L., Benson, S.M., 2012. Relative permeability and trapping of CO₂ and water in sandstone rocks at reservoir conditions. *Water Resour. Res.* 48, W02532.

- Kruschke, J., 2014. Doing Bayesian data analysis: A tutorial with R, JAGS, and Stan. Academic Press.
- Li, C., Laloui, L., 2016. Coupled multiphase thermo-hydro-mechanical analysis of supercritical CO₂ injection: Benchmark for the In Salah surface uplift problem. *Int. J. Greenh. Gas Control.* 51, 394–408.
- Liu, M., Grana, D., 2020. Petrophysical characterization of deep saline aquifers for CO₂ storage using ensemble smoother and deep convolutional autoencoder. *Adv. Water Resour.* 142, 103634.
- Liu, Y., Durlofsky, L.J., 2021. 3D CNN-PCA: A deep-learning-based parameterization for complex geomodels. *Comput. Geosci.* 148, 104676.
- Metropolis, N., Rosenbluth, A.W., Rosenbluth, M.N., Teller, A.H., Teller, E., 1953. Equation of state calculations by fast computing machines. *J. Chem. Phys.* 21, 1087–1092.
- Mo, S., Zhu, Y., Zabaras, N., Shi, X., Wu, J., 2019. Deep convolutional encoder-decoder networks for uncertainty quantification of dynamic multiphase flow in heterogeneous media. *Water Resour. Res.* 55, 703–728.
- Nicolaidou, E., Birchwood, R.A., Prioul, R., Rodriguez-Herrera, A., 2022. Stochastic inversion of wellbore stability models calibrated with hard and soft data, in: U.S. Rock Mechanics/Geomechanics Symposium, American Rock Mechanics Association.
- Remy, N., Boucher, A., Wu, J., 2009. Applied geostatistics with SGeMS: A user's guide. Cambridge University Press.

- Saadatpoor, E., Bryant, S.L., Sepehrnoori, K., 2010. New trapping mechanism in carbon sequestration. *Transp. Porous Media.* 82, 3–17.
- Sun, W., Durlofsky, L.J., 2019. Data-space approaches for uncertainty quantification of CO₂ plume location in geological carbon storage. *Adv. Water Resour.* 123, 234–255.
- Tang, H., Fu, P., Jo, H., Jiang, S., Sherman, C.S., Hamon, F., Azzolina, N.A., Morris, J.P., 2022b. Deep learning-accelerated 3D carbon storage reservoir pressure forecasting based on data assimilation using surface displacement from InSAR. *Int. J. Greenh. Gas Control.* 120, 103765.
- Tang, M., Ju, X., Durlofsky, L.J., 2022a. Deep-learning-based coupled flow-geomechanics surrogate model for CO₂ sequestration. *Int. J. Greenh. Gas Control.* 118, 103692.
- Tang, M., Liu, Y., Durlofsky, L.J., 2020. A deep-learning-based surrogate model for data assimilation in dynamic subsurface flow problems. *J. Comput. Phys.* 413, 109456.
- Tang, M., Liu, Y., Durlofsky, L.J., 2021. Deep-learning-based surrogate flow modeling and geological parameterization for data assimilation in 3D subsurface flow. *Comput. Methods Appl. Mech. Eng.* 376, 113636.
- Tavakoli, R., Yoon, H., Delshad, M., ElSheikh, A.H., Wheeler, M.F., Arnold, B.W., 2013. Comparison of ensemble filtering algorithms and null-space Monte Carlo for parameter estimation and uncertainty quantification using CO₂ sequestration data. *Water Resour. Res.* 49, 8108–8127.

- Wang, N., Chang, H., Zhang, D., 2021. Efficient uncertainty quantification for dynamic subsurface flow with surrogate by theory-guided neural network. *Comput. Methods Appl. Mech. Eng.* 373, 113492.
- Wen, G., Hay, C., Benson, S.M., 2021. CCSNet: a deep learning modeling suite for CO₂ storage. *Adv. Water Resour.* 155, 104009.
- Wen, G., Li, Z., Long, Q., Azizzadenesheli, K., Anandkumar, A., Benson, S.M., 2023. Real-time high-resolution CO₂ geological storage prediction using nested Fourier neural operators. *Energy Environ. Sci.* 16, 1732–1741.
- White, J.A., Chiaramonte, L., Ezzedine, S., Foxall, W., Hao, Y., Ramirez, A., McNab, W., 2014. Geomechanical behavior of the reservoir and caprock system at the In Salah CO₂ storage project. *Proc. Natl. Acad. Sci.* 111, 8747–8752.
- Xiao, C., Zhang, S., Ma, X., Jin, J., Zhou, T., 2022. Model-reduced adjoint-based inversion using deep-learning: Example of geological carbon sequestration modeling. *Water Resour. Res.* 58, e2021WR031041.
- Yan, B., Chen, B., Harp, D.R., Jia, W., Pawar, R.J., 2022a. A robust deep learning workflow to predict multiphase flow behavior during geological CO₂ sequestration injection and post-injection periods. *J. Hydrol.* 607, 127542.
- Yan, B., Harp, D.R., Chen, B., Hoteit, H., Pawar, R.J., 2022b. A gradient-based deep neural network model for simulating multiphase flow in porous media. *J. Comput. Phys.* 463, 111277.

Zhou, Z., Tartakovsky, D.M., 2021. Markov chain Monte Carlo with neural network surrogates: application to contaminant source identification. Stoch. Environ. Res. Risk Assess. 35, 639–651.